A global assessment of effective fracture porosity and density in crystalline rocks

J.M. van den Berg[1,2], E. Luijendijk[1,2], G. Ferguson[3] & O.Warr[4]

[1]Department of Earth Science, University of Bergen, Bergen, Norway

[2]Bjerknes Centre for Climate Research, Bergen, Norway

[3]Department of Civil, Geological and Environmental Engineering and Bjerknes Centre for Climate Research, University of Saskatchewan, Saskatoon, Canada

[4]Department of Earth and Environmental Sciences, University of Ottawa, Ottawa, Canada

Corresponding author: Grant Ferguson (grant.ferguson@usask.ca)

THIS MANUSCRIPT HAS BEEN SUBMITTED TO GEOPHYSICAL RESEARCH LETTERS AND HAS NOT BEEN PEER REVIEWED.

Key Points:

- Effective fracture porosity in crystalline rocks is much lower than commonly assumed values
- Effective porosity and hydraulically active fracture density decrease with depth following a power-law relationship
- Low effective porosity implies reduced groundwater storage and stronger fluid isolation

Abstract

Knowledge of effective fracture porosity in crystalline rocks is important for water resources, geological storage and subsurface biogeochemistry, but remains poorly constrained due to limited and regionally biased data. Here, we use global permeability datasets and equations that relate effective porosity and permeability to estimate effective porosity and hydraulically active fracture density for 27,966 points globally. The resulting global effective porosity distributions are right-skewed and show a power-law decrease with depth. The median and mean effective porosity values are much lower than previously assumed. The natural variability in effective porosity is much larger than parameter uncertainty, underscoring the robustness of our global trends. Low effective porosity implies enhanced fluid isolation in the crystalline crust, with implications for hydrogen and helium accumulation and the deep biosphere.

1 Introduction

Fracture properties such as effective porosity (the pore space contributing to fluid storage and flow (Bear, 1972) and hydraulically active fracture density are crucial for understanding fluid flow in crystalline rocks and have significant implications for fields like hydrogeology, nuclear waste storage, subsurface energy resources, and the deep biosphere. Because porosity in crystalline rocks is typically low, fractures play a key role in controlling fluid flow (Singhal & Gupta, 2010). As a result, fracture properties strongly influence groundwater circulation, residence times, and hydraulic connectivity. Understanding the distribution of these properties is therefore important for characterizing and predicting fluid flow in crystalline rock environments.

Despite their importance, fracture porosity and hydraulically active fracture density in crystalline rocks remain poorly quantified due to significant measurement challenges and limited, regionally biased datasets. Measuring fracture properties in crystalline rock is often difficult due to both technical and geological constraints. Direct measurement techniques are often costly and time-consuming (Möri et al., 2021; Pouraskarparast et al., 2024) and laboratory measurements are often overestimated due to stress release and sample preparation (Schild et al., 2001).

To our knowledge, most measurements of effective porosity in crystalline rocks are limited to studies mainly from Europe, with values ranging from around 0.2% to 2.3% (e.g. Eliasson, 1993; Holland et al., 2013; Möri et al., 2021; Sardini et al., 2006; Schild et al., 2001). These regional data do not provide a comprehensive picture of effective porosity on a global scale. Studies often use a value of 1% for the effective porosity in crystalline rock, but with limited or no supporting evidence (Banks & Robins, 2002). Furthermore, Higgins et al. (2025) show that measurable primary effective porosity in crystalline rocks often contributes little to hydraulic flow because only a small fraction is connected at scales relevant for groundwater transport. This underscores the need to quantify effective, fracture-controlled effective porosity rather than rely on total effective porosity values.

Knowledge of hydraulically active fracture density is even more scarce, to our knowledge, with existing data mostly from studies in the United States and focused on sedimentary rocks. Reported fracture densities range from less than 0.10 to 10.50 fractures per meter, but these estimates are mainly based on outcrop observations, while data from greater depths remain scarce (e.g. Corbett et al., 1987; Seeburger, 1982; Tokhmchi et al., 2010).

The availability of global permeability datasets present a research opportunity to estimate effective fracture porosity and hydraulically active fracture density using established relations between permeability and effective porosity. Here, we estimate effective fracture porosity and hydraulically active fracture density using a global fracture permeability dataset along with a modified form of Snow's (1968) equation and examine their relation with depth and geological setting.

2 Methods

2.1 Estimating effective porosity from permeability

We modify an equation used by Snow (1968) to calculate fracture porosity from permeability measurements, by adding a term to account for fracture roughness. In addition, we used aperture instead of fracture spacing as the main unknown because more data is available on fracture aperture, although the available data is admittedly still limited. Assuming that all fractures are equal, we get equation 1 (comparable to Equation 6 from Snow (1968)) with permeability k [m^2], the number of fractures in a rock volume n [-], the width of the fracture w [m], and a roughness factor f [-]:

$$k = \frac{n}{W} \frac{1}{12f} b^3 \tag{1}$$

Fracture system effective porosity, ϕ [-], is the volume of fractures divided by the volume of the rock (Singhal & Gupta, 2010). The assumption that all fractures are equal, implies that the total volume of all fractures is equal to the volume of a single fracture multiplied by the number of fractures (*n*) (equation 2). With *w* [m] as fracture width and depth.

$$\phi = \frac{n\, b\, w^2}{W^3} \tag{2}$$

Adding the assumption that a fracture extends through the entire rock volume that is sampled by a permeability test or model (*w*=*W*) simplifies equation 2 and allows us to express it in terms of the number of fractures (*n*) over the width of the rock, which can be substituted in equation 1. Rearranging this provides an equation for effective porosity based on permeability, aperture, and a roughness factor.

$$\phi = k \frac{12f}{b^2} \tag{3}$$

2.1.1 Permeability

We compiled permeability data of fractured crystalline rocks from two major sources. We combined 28,832 datapoints in crystalline rock published by Achtziger-Zupančič et al. (2017) with 756 data points for undisturbed continental crust used by Kuang & Jiao (2014). The data from Achtziger-Zupančič et al. (2017) is compiled from 221 published papers and reports, and consists of permeability values based on in-situ measurements from a wide range of methods. Kuang & Jiao (2014) compiled data from 13 different papers, with permeability values obtained from laboratory measurements, pumping tests, injection tests, analytical modeling, in situ measurements, and numerical models.

The data span a large depth range, from 0.5 meters to 36,000 meters. Manning & Ingebritsen (1999) models indicate that significant permeability may persist well below 10-

15 km, extending into the ductile crust, in tectonically active settings. However, most (98.8%) of our data points are located in the first two kilometers.

For the upper two kilometers, we followed Achtziger-Zupančič et al. (2017) to filter the available datapoints and remove unrealistic, high-uncertainty values and values obtained from simulation tests, see supporting information (text S1.2). There are fewer in-situ measurement data available for depths below two kilometers. Therefore, we used permeability estimates based on model simulations for these depths.

After applying the data filtering steps, the final database contains 27,966 data points. Most of the data (69%) is located in the first 500 meters and 82% of the data points in the first 1000 meters of the subsurface, see supporting information (Figure S1). Although the dataset consolidates data from 28 different countries, see supporting information (Figure S1).

2.1.2 Roughness factor

We used a facture roughness factor to account for the deviations from ideal parallel-plate flow. Based on laboratory measurements from crystalline rocks Witherspoon et al. (1980), we adopted a representative value of 1.21. Uncertainty was incorporated by sampling from the reported range (see supporting information (text S1.3).

2.1.3 Aperture values

We used an equation by Jiang et al. (2010) (equation 4) to quantify the depth dependence of aperture in fractures due to increase in effective stress. We adopted the approach of Jiang et al. (2010) rather than methods such as Bisdom et al. (2016), which require parameters like Joint Roughness Coefficient (JRC) and Joint Compressive Strength (JCS) obtained through fracture surface characterization or laboratory testing. The parameters needed for the aperture equation by Jiang et al. (2010) could be reasonably estimated from bulk rock properties. The relation between aperture and effective stress is given by:

$$b(z) = b_0 - \frac{\sigma_n'}{K_{n0} + (\sigma_n'/(b_0 - b_r))} \tag{4}$$

with b_0 [m] representing the initial aperture, σ_n' [kg m-3] the effective normal stress, K_{n0} [kg s-2] the initial normal stiffness, and b_r [m] the residual aperture. Facture aperture was modeled as a function of depth, accounting for closure under increasing effective stress. Initial aperture values were constrained using literature compilations, with a representative median value of 171 μm. Effective normal stress was estimated from overburden and fluid pressure, assuming typical crustal densities of 2660 kg m^{-3}, geothermal gradients of 25°C km^{-1} and hydrostatic conditions. The initial normal stiffness was assigned a representative value of 5 x 10^9 Pa m^{-1} based on published estimates for crystalline rock (Y. Cheng &

Renner, 2022) and residual aperture was assumed to be 14% of the initial aperture following literature relations (Brabazon et al., 2019; Hakami, 1989, 1995; Iwano & Einstein, 1993, 1995). Further details of the parameter selection, distributions and uncertainty propagation are provided in the supporting information (text S1.4).

2.2 Effective porosity-depth relation

Using equation 3 and the filtered permeability dataset, we calculated 27,966 effective porosity data points, each associated with a depth value. The relation between effective porosity and depth was evaluated using the Spearman rank correlation coefficient (Spearman, 1904).

We tested multiple functional forms and found that a power-law relation provided the best fit. Therefore, we fitted a linear relation between log effective porosity and log depth, following (5

$$log(\phi) = A\, log(z) + B \tag{5}$$

Which can be expressed as:

$$\phi = 10^{B} z^{A} \tag{6}$$

To avoid overestimation at shallow depths, we identified a minimum depth threshold at which the effective porosity predicted by the fitted line deviates by no more than 10% from the median effective porosity datapoints at that depth. We used bootstrapping to quantify the uncertainty of the fitted effective porosity-depth line (equation 5), using 1000 bootstrap iterations.

2.3 Quantification of uncertainty

We used a Monte Carlo analysis (n=1000) by sampling the input parameters, including fracture aperture, effective stress, initial normal stiffness, residual aperture and permeability. Parameter variability and distributions were based on literature constraints (see supporting information (text S1.3-1.4). To account for uncertainty in fracture orientation, we randomly assign an angle between 0 and 90, representing the full possible range of fracture inclinations. Permeability uncertainty was incorporated using a log-uniform range reflecting measurement variability (see supporting information (text S1.5)). Uncertainty was evaluated at both the individual data point level and for the aggregated dataset, using median and interquartile range (IQR) as robust measures for skewed distributions (Efron & Tibshirani, 1994).

2.4 Geological factors influencing effective porosity

We explored correlations between effective porosity tectonic setting (Hasterok et al., 2022), type of plate boundary (Hasterok et al., 2022), and rock type. These variables are available for 98% of the dataset, allowing for a robust analysis of their potential influence on effective porosity. Variable categories with fewer than 150 observations were merged into the ‘other’ category to ensure that each group has enough ranked data to provide meaningful statistical comparisons and stable effect-size estimates.

Differences in effective porosity between groups were assessed using non-parametric tests (Kruskal-Wallis test & Mann-Whitney U test, (Kruskal & Wallis, 1952) and (Mann & Whitney, 1947)), and effect sizes were calculated to quantify the magnitude of these differences. To account for the strong dependence of effective porosity on depth, we also analyzed depth-corrected residuals derived from a global effective porosity-depth relation.

Group-specific effective porosity–depth trends were further evaluated using log–log regression models, and correlations with depth were quantified using Spearman rank coefficients. Full details of statistical methods and tests are provided in the supporting information (text S1.6).

2.5 Hydraulically active fracture density

Using the estimated aperture and effective porosity values, we calculated hydraulically active fracture density, the number of fractures per meter. Hydraulically active fracture density (f_d [m^{-1}]) was estimated assuming effective porosity equals hydraulically active fracture density multiplied by aperture. Rearranging this gives:

$$f_d = \frac{\phi}{b} \tag{7}$$

Note that this assumes that all fractures in the volume that was sampled by the permeability tests have the same aperture. To analyze the relation between hydraulically active fracture density and depth, we applied the same methodology as for effective porosity, including log-log regression, bootstrap uncertainty assessment (n=1000) and depth binning. Details are provided in Section 2.2.

3 Results

3.1 Effective porosity-depth relation

We found a statistically significant negative relation between depth and effective porosity for both for the upper two kilometers ($p < 0.0001$, Spearman $\rho = -0.47$) and the entire depth range ($p < 0.0001$, $\rho = -0.46$). This trend is illustrated Figure 1. The apparent vertical alignment of a subset of data points originates from multiple measurements taken at one location (Masset & Loew, 2010).

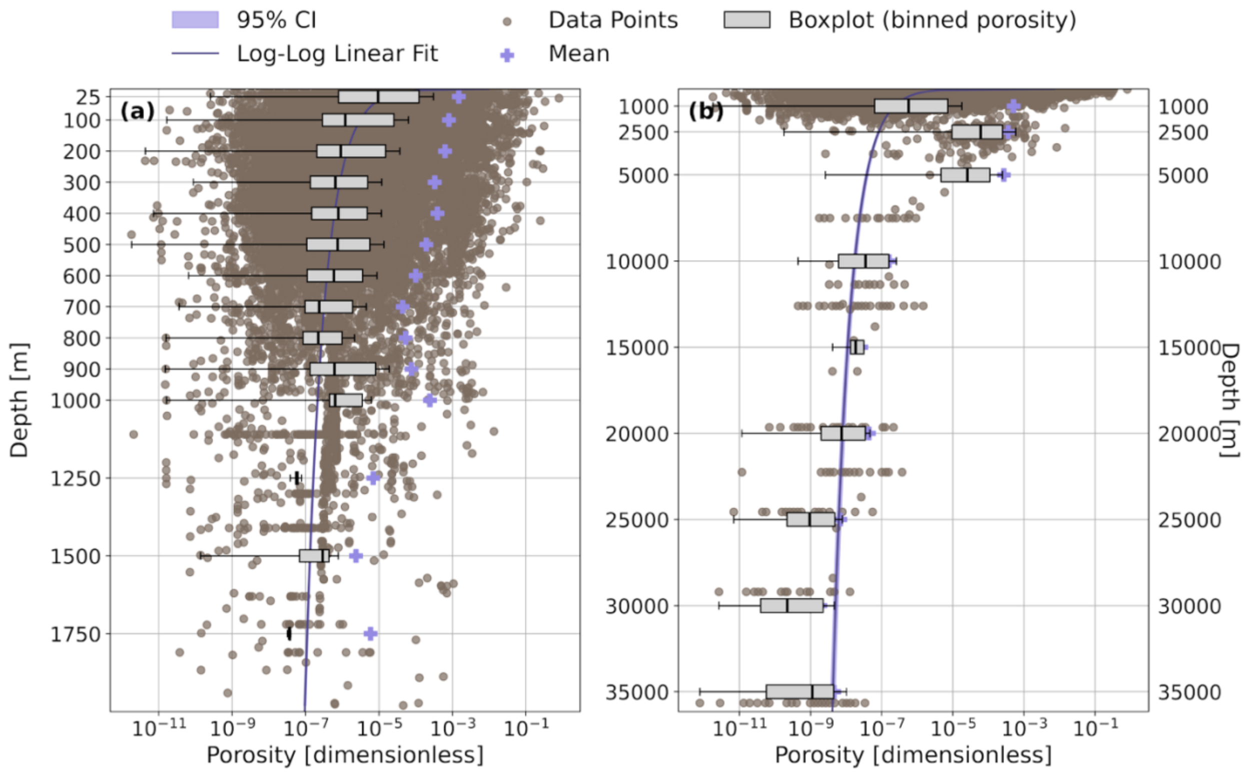

Figure 1. Effective fracture porosity in crystalline rock formations as a function of depth, based on a compilation of effective porosity data points derived from permeability data. a) Upper two kilometers, b) Full depth (0–36,000 m;) Boxplots represent effective porosity distributions within specific depth intervals. A fitted log–log linear regression line is shown, along with a 95% confidence interval. The fit explains 17% of the variance in both cases (R^2 = 0.17).

The fitted linear log-log lines indicate a power-law decrease with depth. Both depth ranges show a similar decrease in effective porosity with depth ($\phi_{0-2\ km} = 10^{-3.17} z^{-1.16}$ and $\phi_{0-36\ km} = 10^{-3.26} z^{-1.12}$ (use from 2 meters deep)). A 250 increase in depth at 250 results in an effective porosity loss of approximately 55%, while the same depth increase at 1000 meters leads to a reduction of around 23%. This indicates that although effective porosity decreases steeply with depth, the rate of decline decreases with increasing depth.

Effective porosity distributions are highly right-skewed across all depth intervals, but become more compact and less influenced by extreme values with increasing depth. Figure 2a-c presents effective porosity distributions across different depth intervals. None of the distributions match common parametric forms (such as exponential, gamma, log-normal and Weibull), indicating no known underlying distribution.

The uncertainty for individual effective porosity estimates (Figure 2d-f) is relatively small compared to the overall variability, indicating that natural heterogeneity dominates. The uncertainty IQR decreases with depth, reflecting the increasing dominance of effective stress in aperture calculations, which reduces the influence of uncertain input parameters. Although both natural variability and parameter uncertainty decrease with depth, the relative contribution of parameter uncertainty becomes more pronounced.

Combining all single-point uncertainty distributions into one aggregated dataset shows that uncertainty has only a modest effect on median and IQR, despite extreme outliers inflating the mean (Figure 2g-i). While the mean increases substantially, the median remains stable (ratios 0.68-1.15), and the IQR increases only slightly (by 33–51%). This indicates that while uncertainty adds some variability, its effect on the overall distribution is modest compared to the natural variability observed in the original data.

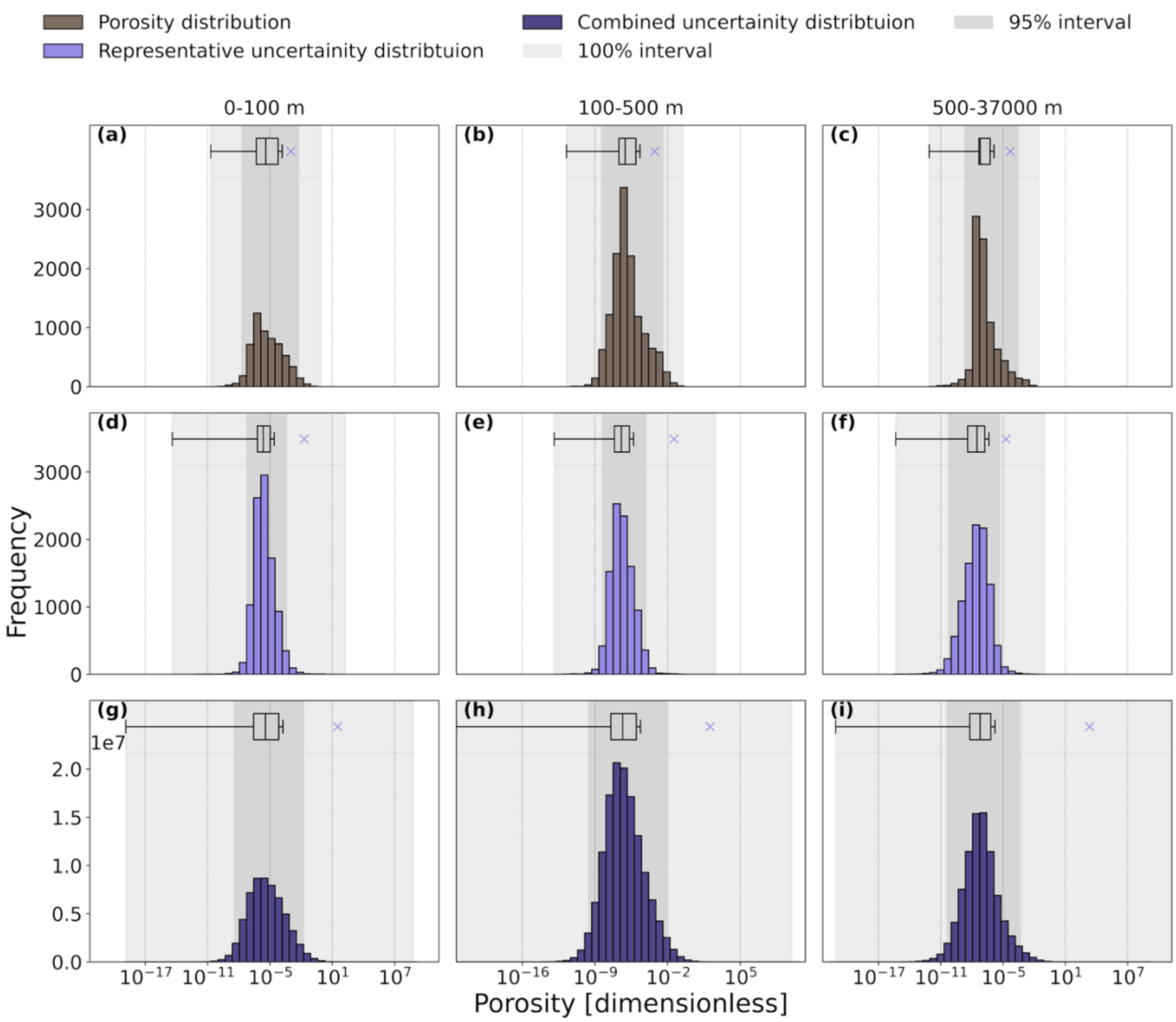

Figure 2. Effective porosity distributions and uncertainty analysis across three depth intervals: 0–100 m, 100–500 m, and 500–36,000 m. a- c: General effective porosity distributions, showing highly right-skewed, non-parametric behavior. d-f: Uncertainty distributions for a representative effective porosity data point, based on Monte Carlo simulations. g-i: Combined uncertainty distributions for all effective porosity points illustrating the overall spread and skewness introduced by input variability.

3.2 Geological factors influencing effective porosity

In addition to depth, geological factors influence effective porosity, although their effect is secondary. Rock type, tectonic setting and the type of plate boundary that is closest to the datapoints all show statistically significant differences in effective porosity distribution; however, most of this variability is small compared to the dominant control of depth. Allowing the porosity-depth relationship to vary among rock types increased the explained variance from 17% to 21.5%, corresponding to a relative increase of about 26% in explained variance.

Among rock types, pegmatite shows the most pronounced positive deviation from the overall effective porosity-depth trend. Similarly, for geological setting, shields, cratons, and accretionary complexes exhibit slightly elevated effective porosity relative to the global trend. The log-log regression model incorporating depth and plate boundary types, compared to just depth, increased the explained variance from 17% to 26%, a relative increase of 52%. In contrast, after accounting for depth, only limited effects remain for plate boundary types, increasing the explained variance of the model with or without plate boundary types relatively only with 6.5%.

Overall, these results indicate that geological factors introduce secondary variability, but do not substantially alter the global effective porosity–depth relation. Details of statistical analyses and group-specific trends are provided in the supporting information (text S2.1).

3.3 Hydraulically active fracture density

Hydraulically active fracture density decreases significantly with depth ($p < 0.0001$, Spearman $\rho \approx -0.35$) for both the upper two kilometers and the entire depth range (Figure 4). This trend indicates that the decrease in effective porosity with depth (Figure 1) cannot be attributed solely to the decrease in fracture aperture with depth but also to a statistically significant decrease in hydraulically active fracture density with depth.

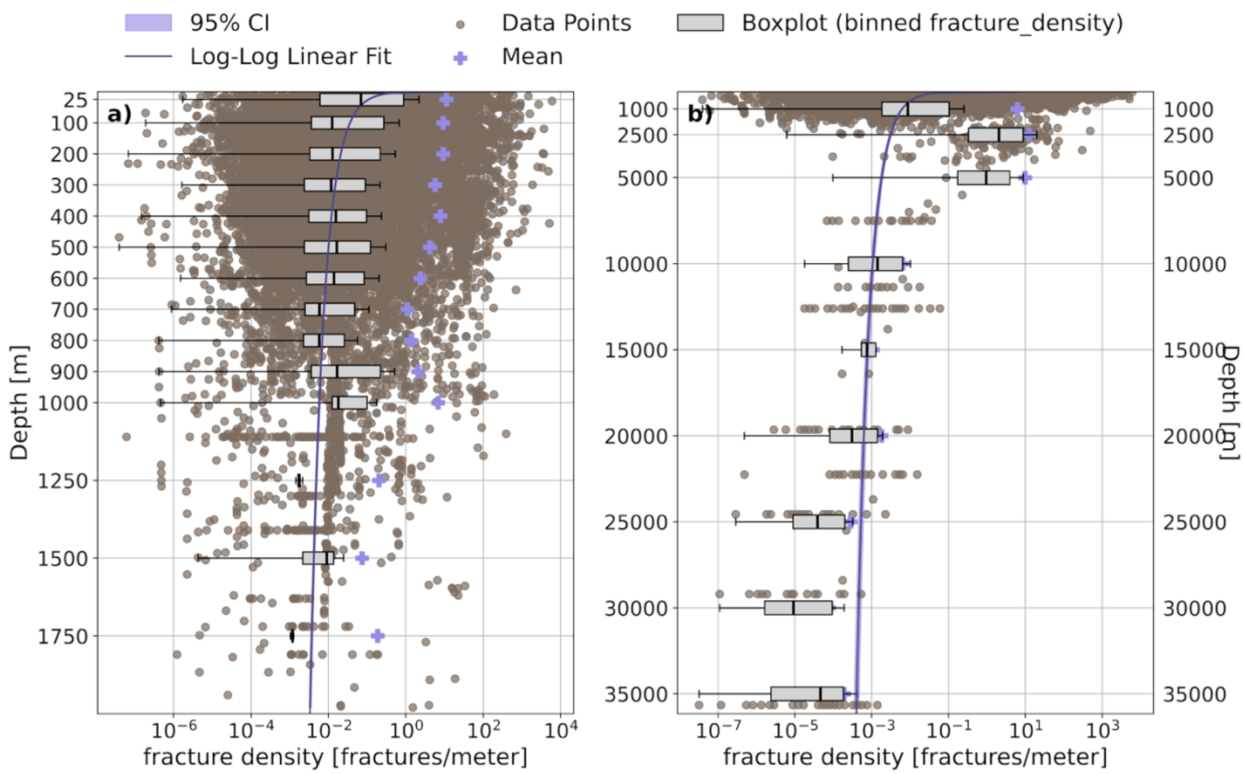

Figure 3. Hydraulically active fracture density in crystalline rock formations as a function of depth a) 0–2,000 m; n = 27,666 b) Full depth range (0–36,000 m; n = 27,966). Boxplots represent effective porosity distributions within specific depth intervals. A fitted log–log linear regression line is shown, along with a 95% confidence interval. The fit explains 9% of the variance in both cases (R^2 = 0.09).

Similar to the effective porosity depth trend, hydraulically active fracture density also decreases with depth following a power-law relationship. However, the decline in hydraulically active fracture density is less steep than that of effective porosity, indicating that fractures tend to narrow more rapidly than they are removed.

The hydraulically active fracture density distributions are right-skewed across all depth intervals (see supporting information (text S2.2)), with variability decreasing at greater depths. As in the effective porosity data, median values are substantially lower than the means, reflecting the influence of extreme outliers.

4. Discussion

4.1 Effective porosity values

Our results showed a right-skewed effective porosity distribution with large differences between the median and mean, which is mainly due to some extreme outliers.

Similar skewness is observed in the storage coefficient data derived from pumping tests in crystalline aquifers, compiled by Boisson et al. (2026). Analysis of this dataset reveals that median storage coefficients are substantially lower than means, closely resembling the skewed effective porosity distributions we observed.

The highly skewed distribution of effective porosity is important when estimating effective porosity for locations or larger regions. For global estimates by Gleeson et al. (2016) or Ferguson et al. (2021), the mean effective porosity can be used as a first-order estimate of the groundwater stored in crystalline rocks. However, when estimating effective porosity at single locations the most likely value is the median of the global effective porosity distribution, which is several orders of magnitude lower.

Reported connected effective porosity (pore space forming continuous pathways for flow) values for crystalline rocks in the literature (typically 0.20%-0.45%) are several orders of magnitude higher than our estimates. This discrepancy likely reflects both methodological and regional biases. Existing datasets are dominated by studies from Scandinavia, which may not be globally representative and laboratory measurements can overestimate effective porosity due to sample disturbance and stress release (Skagius & Neretnieks (1986), Ota et al. (2003)). Furthermore, the literature values represent connected pore effective porosity at sample scale, whereas our estimates reflect effective porosity associated with fracture networks that actively contribute to fluid flow at larger scales. This let us conclude that effective porosity might be far below commonly assumed effective porosity values. This is consistent with site-specific analyses. Higgins et al. (2025) showed that crystalline rocks have measurable primary effective porosity but extremely limited connected pore volume, with secondary effective porosity orders of magnitude lower.

4.2 Geological factors influencing effective porosity

Our observed effective porosity–depth relation is substantially steeper than those reported in previous studies, indicating a stronger depth dependence in crystalline rocks than previously thought. Compared to estimates by Ingebritsen & Manning (2003) and Vitovtova et al. (2014), our results show a faster decline in effective porosity with depth. This difference likely reflects the use of a larger and more representative global dataset, whereas previous studies relied on smaller datasets or simulated conditions.

The crustal effective porosity model from Bethke (1985) is widely applied in studies of fluid flow and crustal gases (e.g., (Sherwood Lollar et al., 2014). Our results indicate a much steeper decrease in effective porosity, with comparable reductions occurring over significantly shorter depth intervals. This discrepancy likely arises because the effective porosity–depth relations underlying the Bethke (1985) model are derived from sedimentary basin compaction models and represent bulk matrix effective porosity, whereas our estimates reflect fracture-controlled, hydraulically effective porosity in crystalline rocks. The steeper decline observed in our dataset compared to previous models indicates that depth exerts a stronger control on fracture-controlled effective porosity than previously assumed.

While a previous study from Ferguson et al. (2023a) has assumed limited or no depth dependence in permeability at depths greater than one kilometer, our results here suggest a depth trend in effective porosity. This difference might arise because effective porosity depends not only on permeability but also on fracture aperture, which decreases systematically with depth in our model. As a result, even in the absence of a strong permeability-depth trend, porosity can exhibit a decrease with depth.

Although depth remains the dominant control, geological factors are important as well, rock type and geological setting explain part of the variability in the data. This was also observed by Achtziger-Zupančič et al. (2017) and Ranjram et al. (2015). It is important to note that in our study, each geological factor was tested independently, although their categories may overlap. Each variable, therefore, represents an isolated comparison, and differences should not be interpreted as additive or combinable across variables.

To calculate effective porosity, we relied on several simplifying assumptions that introduce uncertainty. We assumed that all fractures that contribute to a single permeability measurement are equal in size and properties and that they extend through the entire rock volume considered. Natural fracture systems are highly heterogeneous, with variable lengths, apertures, and connectivity, which can lead to significant deviations from our estimates. Second, we assumed isotropic permeability; however, fracture networks are often anisotropic, with preferential orientations that strongly influence flow paths and connectivity. These assumptions were necessary to enable global-scale analysis using limited data, but they may overestimate connectivity and underestimate travel times in site-specific applications. Future work should incorporate fracture orientation, size variability, and network connectivity to better capture the complexity of fluid flow in crystalline rocks.

4.3 Hydraulically active fracture density

Our hydraulically active fracture density estimates for crystalline rocks are much lower than values reported in the literature, which is based exclusively on sedimentary rocks and therefore offers only a limited basis for comparison. Reported values range from 0.11 to 10.50 fractures per meter, reflecting strong dependence on lithology, scale and measurement method. Seeburger (1982) reported hydraulically active fracture densities of 0.085-0.6 fractures m^{-1} (median: 0.28 fractures m^{-1}) from wells. For the same depth range (0-200 m), our crystalline rock data indicate an eight times lower median of 0.035. However, when comparing data from the same geographic region, our median hydraulically active fracture density is only about two times lower than the values reported by Seeburger (1982). Given that hydraulically active fracture density can vary strongly with observation scale (Marrett et al., 2006), these relatively low hydraulically active fracture densities may reflect either a genuinely sparse fracture network or limitations in the resolution and sensitivity of the permeability-based estimation method. Our method provides the density of fractures that are hydraulically active, i.e. that channel groundwater flow and contribute to permeability, and excludes non-connected fractures that are often included in outcrop or well studies. One of the few studies who are performed on crystalline rock is Johnson (1999), who found a mean fracture density of around 0.47 fractures per meter, based on borehole imaging. This is approximately 14 times greater than the median fracture density of 0.033 fractures per meter we estimated in this study. This difference is expected because borehole imaging records all visible fractures, whereas our estimates represent only fractures contributing to groundwater flow. Long & Witherspoon (1985) showed that hydraulic behavior in fractured rock is controlled by the connectivity of fractures, rather than by the number of fractures present. Consequently, only hydraulically connected fractures contribute to effective porosity.

The equation and input data used to estimate hydraulically active fracture density in our study relies on several simplifying assumptions like uniform fractures and neglect key geometric and structural factors. Our hydraulically active fracture density estimates must be interpreted with caution due to these methodological limitations. However, despite these limitations, this study provides the first attempt to quantify hydraulically active fracture density in the subsurface at the global scale known to us.

4.4 Implications

One of the key outcomes of this study is that the degree to which fracture-associated effective porosity in crystalline settings is considerably lower than previous estimates of porosity global studies (Ferguson et al., 2021; Gleeson et al., 2016; Warr et al., 2018). This finding is in line with other recent studies on the regional (Higgins et al., 2025) and global scales (Ferguson et al., 2023b). The effective porosity evaluated in our study should be interpreted as a minimum estimate of the overall porosity which may still be considerably larger. The highest mean effective porosity calculated here of 0.105 % (0–100 m interval) indicates that, at most, the porosity in connected fractures may represent a maximum of 10% of the entire porosity compared to the in hydrogeologic studies frequently applied value of 1%.

With groundwaters in crystalline rock representing as much as 30% of all terrestrial groundwater (Ferguson et al., 2021; Warr et al., 2018), this would support independent geochemical studies that demonstrate that groundwaters in these settings have the potential to remain in isolation for millions to even billions of years (Heard et al., 2018; Holland et al., 2013; Kietäväinen et al., 2014; Sherwood Lollar et al., 2024; Warr et al., 2018, 2022).

The very low effective porosity values reported here can have important implications for fluid flow in crystalline rock. If flow rate, or hydraulic gradient and permeability, are kept constant or are known, lower effective porosity leads to higher groundwater velocities and shorter travel times (Ingebritsen et al., 2006). However, determining appropriate effective porosities for use in an equivalent porous media models is challenging without tracer data (Worthington, 2022). As a result, it is unclear how to scale the porosities estimated here for use in solute transport problems.

The generation of economically viable deposits of hydrogen and helium in fractured crystalline rocks also depends on porosity and connectivity with the latter potentially promoting migration of hydrogen and helium from deep crystalline settings into overlying lithologies via diffusion through static fluids (A. Cheng et al., 2021; Flude et al., 2025; Sherwood Lollar et al., 2024; Torgersen, 1989). The relatively low connectivity suggested here may simultaneously promote the generation of large volumes of hydrogen and helium in relative isolation while also promoting preferential migration and accumulation in more concentrated localities than previously considered.

Fluids in fractured crystalline rocks may sustain a vast and diverse chemosynthetic-based ecosystem that depends on water rock interactions Bomberg et al. (2021) and Templeton & Caro (2023) and is controlled by the distribution, residence times and connectivity of fluids Templeton & Caro (2023). Consequently, our findings have implications for understanding how, where, and how much life may be sustained, the timescales involved, and the communication between microbial communities.

5. Conclusions

This study provides a first global assessment of effective fracture porosity in crystalline rock. Our results indicate mean values of 0.11% and median values of 4.03 $\times 10^{-4}$%, for the upper 100 meters. These values are several orders of magnitude lower than previously reported effective porosity values, or the commonly assumed value of 1% for total porosity. Our results can be considered a lower bound on total porosity, as they represent only the connected, hydraulically effective fraction of pore space.

Depth is the primary control on effective porosity and explains approximately 17% of the variability of effective porosity. This power-law decline in effective porosity exceeds what would be expected from aperture closure under increasing overburden stress, and reflects the additional influence of the decrease in hydraulically active fracture density with depth. In addition to depth, rock type and geological setting introduce small but statistically significant variability at the global scale.

Our effective porosity estimates represent only a small fraction of the total porosity commonly assumed in crustal models. The low degree of connectivity further supports the potential for long-term fluid isolation in crystalline crust outside of connected fractures, with important implications for groundwater systems, hydrogen and helium accumulation and the deep biosphere.

Acknowledgments

We thank the authors of the original datasets used in this study and William Helland-Hansen (University of Bergen) for valuable discussions. JMvdB was supported by funding from the University of Bergen. GF and OW were supported by the Natural Sciences and Engineering Research Council of Canada Discovery program. OW is a CIFAR Azrieli Global Scholar. This research did not receive specific external funding.

Data availability

The permeability data used in this study are derived from previously published datasets (Achtziger-Zupančič et al., 2017; Kuang & Jiao, 2014). The processed dataset and derived effective porosity and hydraulically active fracture density estimates are publicly available through van den Berg and Luijendijk (2026). The code used for analysis is available at GitHub: https://github.com/JosseBergUiB/global_fracture_porosity.git.

Conflict of interest

The authors declare no conflicts of interest.

References

Achtziger-Zupančič, P., Loew, S., & Mariéthoz, G. (2017). A new global database to improve predictions of permeability distribution in crystalline rocks at site scale. *Journal of Geophysical Research: Solid Earth*, *122*(5), 3513–3539. https://doi.org/10.1002/2017JB014106

Banks, D., & Robins, N. (2002). *An introduction to Groundwater in Crystalline Bedrock*.

Bear, J. (1972). Dynamics of Fluids in Porous Media (Dover Civil and Mechanical Engineering). *Published in 1972 Reprint in 1988 in New York NY) by Dover*, 312–324. https://books.google.com/books/about/Dynamics_of_Fluids_in_Porous_Media.html?hl=no&id=lurrmlFGhTEC

Bethke, C. M. (1985). A numerical model of compaction-driven groundwater flow and heat transfer and its application to the paleohydrology of intracratonic sedimentary basins. *Journal of Geophysical Research*, *90*(B8), 6817–6828. https://doi.org/10.1029/JB090IB08P06817

Bisdom, K., Bertotti, G., & Nick, H. M. (2016). The impact of different aperture distribution models and critical stress criteria on equivalent permeability in fractured rocks. *Journal of Geophysical Research: Solid Earth*, *121*(5), 4045–4063. https://doi.org/10.1002/2015JB012657

Boisson, A., Lucassou, F., Schroëtter, J.-M., Boivin, B., Aertgeerts, G., Venville, M., de Dreuzy, J.-R., Abhervé, R., Armandine Les Landes, A., Rouxel, E., Idée, E., & Mougin, B. (2026). A database of pumping tests in crystalline rocks: Lithostratigraphic controls on transmissivity and its log-normal distribution (Armorican Massif, France). *Journal of Hydrology: Regional Studies*, *65*, 103406. https://doi.org/10.1016/J.EJRH.2026.103406

Bomberg, M., Miettinen, H., Kietäväinen, R., Purkamo, L., Ahonen, L., & Vikman, M. (2021). Microbial metabolic potential in deep crystalline bedrock. *The Microbiology of Nuclear Waste Disposal*, 41–70. https://doi.org/10.1016/B978-0-12-818695-4.00003-4

Brabazon, J. W., Perfect, E., Gates, C. H., Bilheux, H. Z., Tyner, J. S., McKay, L. D., & Horodecky, B. B. (2019). Rock Fracture Sorptivity as Related to Aperture Width and Surface Roughness. *Vadose Zone Journal*, *18*(1), 1–10. https://doi.org/10.2136/VZJ2018.08.0156

Cheng, A., Sherwood Lollar, B., Warr, O., Ferguson, G., Idiz, E., Mundle, S. O. C., Barry, P. H., Byrne, D. J., Mabry, J. C., & Ballentine, C. J. (2021). Determining the role of diffusion and basement flux in controlling 4He distribution in sedimentary basin fluids. *Earth and Planetary Science Letters*, *574*, 117175. https://doi.org/10.1016/J.EPSL.2021.117175

Cheng, Y., & Renner, J. (2022). Estimation of fracture normal stiffness using wellbore pressure recovery. *Geophysical Journal International*, *232*(1), 223–246. https://doi.org/10.1093/GJI/GGAC295

Corbett, K., Friedman, M., & Spang', J. (1987). *Fracture Development and Mechanical Stratigraphy of Austin Chalk, Texas^* (Vol. 71, Number 1). Tables. http://pubs.geoscienceworld.org/aapg/aapgbull/article-pdf/71/1/17/4459257/aapg_1987_0071_0001_0017.pdf

Efron, B., & Tibshirani, R. J. (1994). An Introduction to the Bootstrap. *An Introduction to the Bootstrap*. https://doi.org/10.1201/9780429246593/INTRODUCTION-BOOTSTRAP-BRADLEY-EFRON-TIBSHIRANI

Eliasson, T. (1993). *Mineralogy, geochemistry and petrophysics of red coloured granite adjacent to fractures SVENSK KÄRNBRÄNSLEHANTERING AB SWEDISH NUCLEAR FUEL AND WASTE MANAGEMENT CO*.

Ferguson, G., McIntosh, J. C., Warr, O., Sherwood Lollar, B., Ballentine, C. J., Famiglietti, J. S., Kim, J. H., Michalski, J. R., Mustard, J. F., Tarnas, J., & McDonnell, J. J. (2021). Crustal Groundwater Volumes Greater Than Previously Thought. *Geophysical Research Letters*, *48*(16). https://doi.org/10.1029/2021GL093549

Ferguson, G., McIntosh, J., Warr, O., & Sherwood Lollar, B. (2023a). The low permeability of the Earth's Precambrian crust. *Communications Earth & Environment 2023 4:1*, *4*(1), 323-. https://doi.org/10.1038/s43247-023-00968-2

Ferguson, G., McIntosh, J., Warr, O., & Sherwood Lollar, B. (2023b). The low permeability of the Earth's Precambrian crust. *Communications Earth & Environment 2023 4:1*, *4*(1), 323-. https://doi.org/10.1038/s43247-023-00968-2

Flude, S., Warr, O., Magalhães, N., Bordmann, V., Fleury, J.-M., Reis, H., Trindade, R., Hillegonds, D., T. Rodrigues, R., Piatti, B., Holdship, P., Sherwood Lollar, B., & Ballentine, C. J. (2025). Generation, migration and accumulation of natural hydrogen and helium in the intracratonic São Francisco Basin, eastern Brazil: implications for the understanding and exploration of natural H 2 systems . *Geoenergy*, *3*(1). https://doi.org/10.1144/GEOENERGY2024-042/ASSET/26D4EEE3-0144-4C2D-959D-B77F060E3839/ASSETS/IMAGES/LARGE/GEOENERGY2024-042.11.JPG

Gleeson, T., Befus, K. M., Jasechko, S., Luijendijk, E., & Cardenas, M. B. (2016). The global volume and distribution of modern groundwater. *Nature Geoscience*, *9*, 161–167. https://doi.org/10.1038/NGEO2590

Gross, M. R. (1993). The origin and spacing of cross joints: examples from the Monterey Formation, Santa Barbara Coastline, California. In *Journal of Structural Geology* (Vol. 15, Number 6).

Hakami, E. (1989). *RUCI Water Flow in Single Rock Joints SWEDISH NUCLEAR FUEL AND WASTE MANAGEMENT CO Division of Research and Development*.

Hakami, Eva. (1995). *Aperture distribution of rock fractures*. Kungl. Tekniska högskolan.

Hasterok, D., Halpin, J. A., Collins, A. S., Hand, M., Kreemer, C., Gard, M. G., & Glorie, S. (2022). New Maps of Global Geological Provinces and Tectonic Plates. *Earth-Science Reviews*, *231*, 104069. https://doi.org/10.1016/J.EARSCIREV.2022.104069

Heard, A. W., Warr, O., Borgonie, G., Linage, B., Kuloyo, O., Fellowes, J. W., Magnabosco, C., Lau, M. C. Y., Erasmus, M., Cason, E. D., van Heerden, E., Kieft, T. L., Mabry, J. C., Onstott, T. C., Sherwood Lollar, B., & Ballentine, C. J. (2018). South African crustal fracture fluids preserve paleometeoric water signatures for up to tens of millions of years. *Chemical Geology*, *493*, 379–395. https://doi.org/10.1016/J.CHEMGEO.2018.06.011

Higgins, P. M., Song, M., Warr, O., & Sherwood Lollar, B. (2025). Natural H2 and Sulfate Production via Radiolysis in Low Porosity and Permeability Crystalline Rocks. *Journal of Geophysical Research: Biogeosciences*, *130*(6), e2025JG008863. https://doi.org/10.1029/2025JG008863

Holland, G., Lollar, B. S., Li, L., Lacrampe-Couloume, G., Slater, G. F., & Ballentine, C. J. (2013). Deep fracture fluids isolated in the crust since the Precambrian era. *Nature 2013 497:7449*, *497*(7449), 357–360. https://doi.org/10.1038/nature12127

Ingebritsen, S. E., & Manning, C. E. (2003). Implications of crustal permeability for fluid movementbetween terrestrial fluid reservoirs. *Journal of Geochemical Exploration*, *78–79*, 1–6. https://doi.org/10.1016/S0375-6742(03)00037-2

Ingebritsen, S. E., Sanford, W. E., & Neuzil, C. E. (2006). *Groundwater in Geologic Processes* (2nd ed.). Cambridge University Press. www.cambridge.org

Iwano, M., & Einstein, H. H. (1993). *Stochastic analysis of surface roughness, aperture and flow in a single fracture*. *90*, 54103396. http://onepetro.org/ISRMEUROCK/proceedings-pdf/EUROCK93/All-EUROCK93/ISRM-EUROCK-1993-018/1978203/isrm-eurock-1993-018.pdf

Iwano, M., & Einstein, H. H. (1995). *Hydromechanical Characteristics of a Single Rock Joint*.

Jiang, X.-W., Wang, X.-S., & Wan, L. (2010). Semi-empirical equations for the systematic decrease in permeability with depth in porous and fractured media. *Hydrogeology Journal*, *18*(4), 839–850. https://doi.org/10.1007/S10040-010-0575-3/FIGURES/5

Johnson, C. D. (1999). *Effects of Lithology and Fracture Characteristics on Hydraulic Properties in Crystalline Rock: Mirror Lake Research Site, Grafton County, New Hampshire*.

Kietäväinen, R., Ahonen, L., Kukkonen, I. T., Niedermann, S., & Wiersberg, T. (2014). Noble gas residence times of saline waters within crystalline bedrock, Outokumpu Deep Drill Hole, Finland. *Geochimica et Cosmochimica Acta*, *145*, 159–174. https://doi.org/10.1016/J.GCA.2014.09.012

Kruskal, W. H., & Wallis, W. A. (1952). Use of Ranks in One-Criterion Variance Analysis. *Journal of the American Statistical Association*, *47*(260), 583. https://doi.org/10.2307/2280779

Kuang, X., & Jiao, J. J. (2014). An integrated permeability-depth model for Earth's crust. *Geophysical Research Letters*, *41*(21), 7539–7545. https://doi.org/10.1002/2014GL061999

Long, J. C. S., & Witherspoon, P. A. (1985). The Relationship of the Degree of Interconnection to Permeability in Fracture Networks. *JOURNAL OF GEOPHYSICAL RESEARCH*, *90*(B4), 3087–3098. https://doi.org/10.1029/JB090iB04p03087

Lorenz, J. C., Nat, S., Hili, R. E., & Corp, C. (1994). *Subsurface Fracture Spacing: Comparison of Inferences From Slant/Horizontal and Vertical Cores*. http://onepetro.org/FE/article-pdf/9/01/66/2605014/spe-21877-pa.pdf/1

Mann, H. B., & Whitney, D. R. (1947). On a Test of Whether one of Two Random Variables is Stochastically Larger than the Other. *Source: The Annals of Mathematical Statistics*, *18*(1), 50–60.

Manning, C. E., & Ingebritsen, S. E. (1999). Permeability of the continental crust: Implications of geothermal data and metamorphic systems. *Reviews of Geophysics*, *37*(1), 127–150. https://doi.org/10.1029/1998RG900002

Marrett, R. A., Laubach, S. E., of Economic Geology, B., Jackson, K. G., & Ortega, O. J. (2006). A scale-independent approach to fracture intensity and average spacing measurement. *AAPG Bulletin*, *90*(2), 193–208. https://doi.org/10.1306/08250505059

Masset, O., & Loew, S. (2010). Distribution de la conductivité hydraulique dans des roches cristallines, déduite des flux entrants dans des tunnels et galeries des Alpes centrales, Suisse. *Hydrogeology Journal*, *18*(4), 863–891. https://doi.org/10.1007/S10040-009-0569-1/FIGURES/21

Möri, A., Mazurek, M., Ota, K., Siitari-Kauppi, M., Eichinger, F., & Leuenberger, M. (2021). Quantifying the Porosity of Crystalline Rocks by In Situ and Laboratory Injection Methods. *Minerals 2021, Vol. 11, Page 1072*, *11*(10), 1072. https://doi.org/10.3390/MIN11101072

Narr, W. (1996). Estimating Average Fracture Spacing in Subsurface Rock. *AAPG Bulletin*, *10*(80), 1565–1585. https://doi.org/https://doi.org/10.1306/64EDA0B4-1724-11D7-8645000102C1865D

Narr, W., & Suppe, J. (1991). Joint spacing in sedimentary rocks. In *Journal of Structural Geology* (Vol. 13, Number 9).

Ota, K., Möri, A., Alexander, W. R., Frieg, B., & Schild, M. (2003). Influence of the mode of matrix porosity determination on matrix diffusion calculations. *Journal of Contaminant Hydrology*, *61*(1–4), 131–145. https://doi.org/10.1016/S0169-7722(02)00139-0

Pouraskarparast, Z., Aghaei, H., Colombera, L., Masoero, E., & Ghaedi, M. (2024). Fracture aperture: A review on fundamental concepts, estimation methods, applications, and research gaps. In *Marine and Petroleum Geology* (Vol. 164). Elsevier Ltd. https://doi.org/10.1016/j.marpetgeo.2024.106818

Ranjram, M., Gleeson, T., & Luijendijk, E. (2015). Is the permeability of crystalline rock in the shallow crust related to depth, lithology or tectonic setting? *Geofluids*, *15*(1–2), 106–119. https://doi.org/10.1111/GFL.12098

Sardini, P., Siitari-Kauppi, M., Beaufort, D., & Hellmuth, K. H. (2006). On the connected porosity of mineral aggregates in crystalline rocks. *American Mineralogist*, *91*(7), 1069–1080. https://doi.org/10.2138/AM.2006.1939

Schild, M., Siegesmund, S., Vollbrecht, A., & Mazurek, M. (2001). Characterization of granite matrix porosity and pore-space geometry by in situ and laboratory methods. *Geophysical Journal International*, *146*(1), 111–125. https://doi.org/10.1046/J.0956-540X.2001.01427.X/2/146-1-111-FIG013.JPEG

Seeburger, D. A. (1982). The Distribution of Natural Fractures and Joints at Depth in Crystalline Rock. *JOURNAL OF GEOPHYSICAL RESEARCH*, *87*(B7), 5517–5534. https://doi.org/10.1029/JB087iB07p05517

Sherwood Lollar, B., Onstott, T. C., Lacrampe-Couloume, G., & Ballentine, C. J. (2014). The contribution of the Precambrian continental lithosphere to global H2 production. *Nature 2014 516:7531*, *516*(7531), 379–382. https://doi.org/10.1038/nature14017

Sherwood Lollar, B., Warr, O., & Higgins, P. M. (2024). The Hidden Hydrogeosphere: The Contribution of Deep Groundwater to the Planetary Water Cycle. *Annual Review of Earth and Planetary Sciences*, *52*(1), 443–466. https://doi.org/10.1146/ANNUREV-EARTH-040722-102252/CITE/REFWORKS

Singhal, B. B. S., & Gupta, R. P. (2010). Applied hydrogeology of fractured rocks: Second edition. In *Applied Hydrogeology of Fractured Rocks: Second Edition*. Springer Netherlands. https://doi.org/10.1007/978-90-481-8799-7

Skagius, K., & Neretnieks, I. (1986). Porosities and Diffusivities of Some Nonsorbing Species in Crystalline Rocks. *WATER RESOURCES RESEARCH*, *22*(3), 389–398. https://doi.org/10.1029/WR022i003p00389

Smellie, J., Waber, N., & Frape, S. (2003). *Matrix fluid chemistry experiment. Final report June 1998 - March 2003.* https://inis.iaea.org/records/avmgj-jv035

Snow, D. T. (1968). Rock Fracture Spacings, Openings, and Porosities. *Journal of the Soil Mechanics and Foundations Division*, *94*(1), 73–91. https://doi.org/10.1061/JSFEAQ.0001097

Spearman, C. (1904). The Proof and Measurement of Association between Two Things. *The American Journal of Psychology*, *15*(1), 72. https://doi.org/10.2307/1412159

Stanfors, R., Olsson, P., Stille, H., & Kärnbränslehantering, S. (1996). ÄSPÖ HRL-Geoscientific evaluation 1997/3 Results from pre-investigations and detailed site characterization Comparison of predictions and observations Geology and mechanical stability TECHNICAL REPORT. *CM Gruppen AB*.

Templeton, A. S., & Caro, T. A. (2023). The Rock-Hosted Biosphere. *Annual Review of Earth and Planetary Sciences*, *51*(Volume 51, 2023), 493–519. https://doi.org/10.1146/ANNUREV-EARTH-031920-081957/1

Tokhmchi, B., Memarian, H., & Rezaee, M. R. (2010). Estimation of the fracture density in fractured zones using petrophysical logs. *Journal of Petroleum Science and Engineering*, *72*(1–2), 206–213. https://doi.org/10.1016/J.PETROL.2010.03.018

Torgersen, T. (1989). Terrestrial helium degassing fluxes and the atmospheric helium budget: Implications with respect to the degassing processes of continental crust.

Chemical Geology: Isotope Geoscience Section, *79*(1), 1–14. https://doi.org/10.1016/0168-9622(89)90002-X

Tullborg, E. L., & Larson, S. Å. (2006). Porosity in crystalline rocks – A matter of scale. *Engineering Geology*, *84*(1–2), 75–83. https://doi.org/10.1016/J.ENGGEO.2005.12.001

van den Berg, Josse Maria; Luijendijk, Elco (2026): Global dataset of effective fracture porosity and fracture density estimated from crystalline rock permeability, as a function of depth [dataset]. PANGAEA, https://doi.org/10.1594/PANGAEA.996053

Vitovtova, V. M., Shmonov, V. M., & Zharikov, A. V. (2014). The porosity trend and pore sizes of the rocks in the continental crust of the earth: Evidence from experimental data on permeability. *Izvestiya, Physics of the Solid Earth*, *50*(5), 593–602. https://doi.org/10.1134/S1069351314040181/METRICS

Warr, O., Ballentine, C. J., Onstott, T. C., Nisson, D. M., Kieft, T. L., Hillegonds, D. J., & Sherwood Lollar, B. (2022). 86Kr excess and other noble gases identify a billion-year-old radiogenically-enriched groundwater system. *Nature Communications 2022 13:1*, *13*(1), 3768-. https://doi.org/10.1038/s41467-022-31412-2

Warr, O., Sherwood Lollar, B., Fellowes, J., Sutcliffe, C. N., McDermott, J. M., Holland, G., Mabry, J. C., & Ballentine, C. J. (2018). Tracing ancient hydrogeological fracture network age and compartmentalisation using noble gases. *Geochimica et Cosmochimica Acta*, *222*, 340–362. https://doi.org/10.1016/J.GCA.2017.10.022

Witherspoon, P. A., Wang, J. S. Y., Iwai, K., & Gale, J. E. (1980). Validity of Cubic Law for fluid flow in a deformable rock fracture. *Water Resources Research*, *16*(6), 1016–1024. https://doi.org/10.1029/WR016I006P01016

Worthington, S. R. H. (2022). *Estimating Effective Porosity in Bedrock Aquifers*. https://doi.org/10.1111/gwat.13171

Supporting information for:
A global assessment of effective fracture porosity and density in crystalline rocks

This supporting information provides additional methodological details, data processing steps, and supporting analyses for the main manuscript.

Contents of this file:

Text S1. Methods

S1.1 Elaborate explanation Equation 3 of the paper

We used a form of the cubic law that assumes laminar flow, and includes a roughness factor *f* [-] (Witherspoon et al., 1980). This accounts for fracture surface irregularities. Assuming f≥1, Witherspoon et al. (1980) provide the following equation for the flow rate, *Q* [m^{-3} s^{-1}], per unit hydraulic head, *h* [m], in a single fracture. Note that to account for the direction of flow, a negative sign is introduced in the equation compared to the original equation by Witherspoon et al. (1980):

$$\frac{Q}{\Delta h} = -\frac{C}{f}\, b^3 \tag{S1}$$

b represents the fracture aperture height [m], and *C* is the proportional constant in the cubic law [m^{-1} s^{-1}]. Using these parameters, we can rearrange the equation to calculate the flow rate directly as:

$$Q = -\frac{1}{f}\, C\, b^3\, \Delta h \tag{S2}$$

The total discharge, Q_{total} [m^{-3} s^{-1}], of a rock unit containing several fractures can be expressed as:

$$Q_{total} = \sum_{i=1}^{n} Q_i \tag{S3}$$

With Q_i [m^{-3} s^{-1}] for the flow rate through each fracture. If we assume that all the fractures are equal (assumption 1), the total flow rate is equal to the number of fractures in a rock volume, *n* [-], times the flow rate through these fractures.

$$Q_{total} = -\frac{1}{f} n\ C\ b^3\ \Delta h \quad \text{(S4)}$$

The proportionality constant *C* can be expressed as (Witherspoon et al., 1980):

$$C = \frac{w}{w}\ \frac{\rho g}{12\mu} \quad \text{(S5)}$$

w [m] represents the width and length of the fracture, ρ [kg m^{-3}] fluid density, g [m s^{-2}] acceleration of gravity and μ [kg m^{-1} s^{-1}] fluid viscosity. We replaced *C* in Equation S4.

$$Q_{total} = -\frac{1}{f}\ \frac{\rho g}{12\mu}\ b^3\ n\ \Delta h \quad \text{(S6)}$$

To calculate the total discharge, we could also use Darcy's law (Equation S7). With permeability *k* [m^2], and *W* [m] rock width, height and depth.

$$Q_{total} = -k\ \rho g\ \frac{1}{\mu}\ W^2\ \Delta h\ \frac{1}{W} \quad \text{(S7)}$$

Next, we set Equation S6 equal to Equation S7 .

$$Q_{total} = n\ \frac{1}{f}\ \frac{\rho g}{12\mu}\ b^3 = k\ \rho g\ \frac{1}{\mu}\ W \quad \text{(S8)}$$

$$k = \frac{n}{W}\ \frac{1}{12 f}\ b^3 \quad \text{(S9)}$$

Equation S9 is comparable to Equation 6 from Snow (1968), with a key modification: we introduced a roughness factor. This gave an equation (Equation S9) for permeability, which is given by the number of fractures, the rock extent, the roughness factor, and the aperture. While Snow (1968) chose to reformulate the equation by introducing fracture spacing and removing aperture, we retain aperture in our formulation due to the greater availability and reliability of aperture data.

Fracture system porosity, ϕ [-], is the volume of fractures divided by the volume of the rock (Singhal & Gupta, 2010). Assumption 1 (all fractures are equal) implies that the total volume of all fractures is equal to the volume of a single fracture multiplied by the number of fractures (*n*) (Equation S10). With *w* [m] as fracture width and depth.

$$\phi = \frac{n\ b\ w^2}{W^3} \quad \text{(S10)}$$

Assuming that a fracture extends through the entire rock volume (*w*=*W* - Assumption 2) simplifies Equation S10 and allows us to express it in terms of the number of fractures (*n*) over the width of the rock, *W* (Equation S11).

$$\frac{n}{W} = \frac{\phi}{b} \qquad \text{(S11)}$$

We substituted this in Equation S9, the equation for permeability. Including porosity in the permeability equation (Equation S12).

$$k = \phi \frac{1}{12f} b^2 \qquad \text{(S12)}$$

Rearranging this equation provides a formula for porosity based on permeability, aperture, and a roughness factor.

$$\phi = k \frac{12f}{b^2} \qquad \text{(S13)}$$

Text S1.1.1 Notations

A = slope value [-]

B = intercept [-]

b = aperture height [L]

b_0 = initial aperture width [L]

b_r = residual aperture width [L]

C = proportional constant in cubic law [1/LT]

f = fracture surface characteristic factor [-]

g = acceleration of gravity [L/T^2]

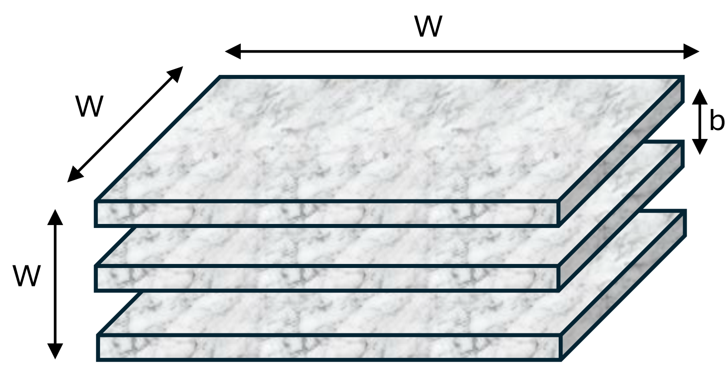

h = hydraulic head [L]

k = permeability [L^2]

K = hydraulic conductivity [L^2/T]

K_{n0} = initial normal stiffness [M/T^2

n = fracture density [-]

Q = flow rate [L^3/T]

w = fracture width and depth [L]

W = rock width, height and depth [L]

z = depth [L]

ρ = fluid density [M/L^3]

μ = flow viscosity [M/LT]

σ_n' = effective normal stress [M/LT^2]

ϕ = porosity [-]

ρ_b = bulk density of the rock [M/L^3]

ρ_{water} = density of water [M/L^3]

θ = the angle of inclination of the fracture [-]

S1.2 Permeability data origin, methods and removal of unrealistic data

Methods used in Achtziger-Zupančič et al. (2017) are hydraulic borehole measurements, pneumatic borehole measurements, pressure tests in tunnels, direct tunnel inflow measurements, indirect determination from seismicity, and calibrated groundwater flow models.

For data filtering, we used the following method: For the upper two kilometers, we followed the method described by Achtziger-Zupančič et al. (2017) to filter the available datapoints and remove unrealistic and high uncertainty values. We excluded data with permeability values at or below the measurement limit and permeability values which were calculated from an interval longer than 100 meters. These values are averaged over large rock sections, making them less reliable. Additionally, following their method, we removed values for which the method used was unclear, as well as those obtained through simulation tests or based on tracer data. Simulation tests were excluded because it often remains uncertain whether the measurements relate to natural or simulated rock mass, and tracer data was discarded because it often infers the permeability of single fractures from numerical and analytical solutions. Additionally, following Achtziger-Zupančič et al. (2017), we excluded unrealistic porosity values (lower than 0 or above 100). There are fewer in-situ measurement data available for depths below two kilometers. Therefore, we did use permeability estimates based on model simulations for these depths.

For the distribution of the data across the depth range and the globe, see Figure S1.

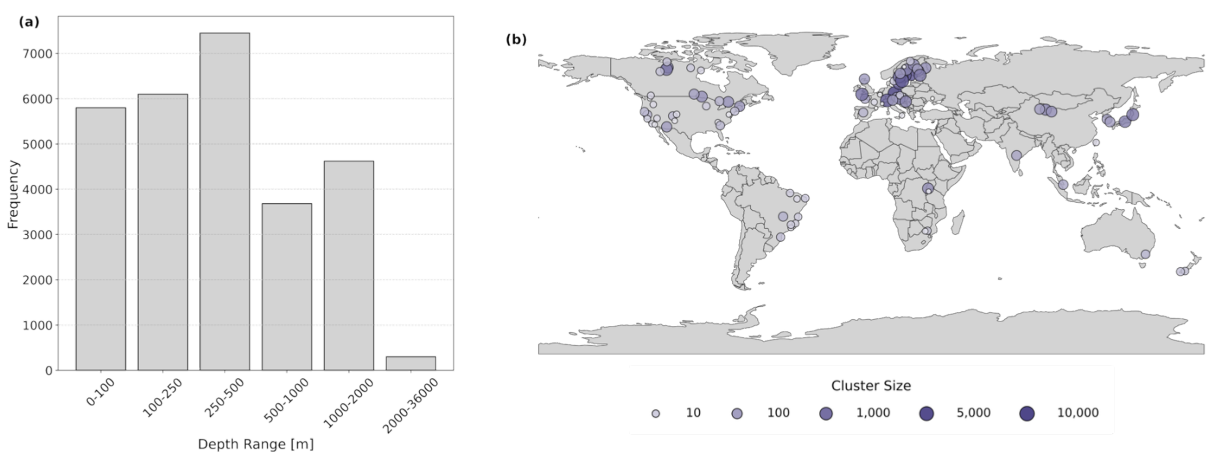

Figure S1. Distribution of effective fracture porosity points by a) depth ranges, and (b) geographic origin by country.

S1.3 Roughness factor

Witherspoon et al. (1980) obtained twelve roughness factor values for granite, marble, and basalt (range: 1.04–1.65, see Figure S2). These values were derived by fitting laboratory flow data to a modified cubic law in which *f* and the residual aperture were determined through least-squares minimization. The roughness factor accounts for the reduction in flow relative to the ideal parallel-plate model caused by surface roughness and contact asperities. To our knowledge, there is no additional information available on the roughness factor in crystalline rocks. Therefore, we assumed a median fracture surface characteristics factor of 1.31 based on the values from Witherspoon et al. (1980).

The roughness values found by Witherspoon et al. (1980) follow a normal distribution. For uncertainty quantification (see 1.5 Quantification of uncertainty) we sampled from a normal distribution defined by the empirical mean and standard deviation of the dataset.

S1.4 Initial aperture parameters

We compiled 27 initial aperture values from the literature (Brabazon et al., 2019; Hakami, 1989, 1995; Iwano & Einstein, 1993, 1995), spanning a range from 43 μm to 650 μm. The median value of 171 μm was used as the initial aperture in Equation 4. The initial aperture values follow a log-normal distribution (see Figure S2 For uncertainty), we sampled from a log-normal distribution.

We calculated the effective stress using (*S14* (Ingebritsen et al., 2006). With ρ_b [kg m^{-3}] representing bulk density of the rock, z [m] the depth, θ [-] the angle of inclination of the fracture and ρ_{water} [kg m^{-3}] density of water. The fracture inclination θ is included because the effective normal stress is calculated on the plane of the fracture, which is typically inclined relative to the vertical. Projecting the vertical overburden stress onto the fracture plane accounts for the component of stress that acts to close the fracture.

$$\sigma_n' = \rho_b \, g \, z \, cos(\theta) - \rho_{water} \, g \, z \quad \text{(S14)}$$

For the bulk density of crystalline rocks in the crust, we used the value 2660 kg m^{-3}, based on the global compilations of laboratory and seismic data on continental crust from Christensen & Mooney (1995). For the fracture angle, we assumed that the fracture angles are randomly distributed in a range between 0- and 90-degree angle and took a median value of 45 degrees angle. Water densities were calculated using Zhang & Duan (2005), using an increase of 25 degrees Celsius per kilometer that represents and average geothermal gradient in the continental crust (Kolawole & Evenick, 2023).

There is minimal literature on the estimation of the initial normal stiffness in crystalline rocks. The only values we found are from Cheng & Renner (2022) for gneisses. Cheng & Renner (2022) estimated the initial normal stiffness for gneisses and found a range of 1.6 x 10^9 – 10^{11} Pa m^{-1}, with a median value of 5 x 10^9 Pa m^{-1}. We adopted this median value for our calculations. We tested the distribution of these inferred values and found them to follow a gamma distribution. For uncertainty quantification, see 1.5 Quantification of uncertainty; we sampled residual aperture values from this distribution. The distribution is illustrated in Figure S2.

To our knowledge, there is no published data on residual aperture values for fractures in crystalline rock. However, Baghbanan & Jing (2008) presented aperture–stress relationships at various depths, from which residual aperture values can be inferred. We estimated that residual aperture typically ranges from 10% to 18% of the initial aperture, with a median of approximately 14%.

To assess the distribution of these values, we tested several known statistical distributions (e.g., normal, log-normal, exponential), but none provided a satisfactory fit. Since no known parametric distribution adequately fit the residual aperture values (see Figure S2), we adopted a non-parametric approach for the uncertainty assessment (see 1.5 Quantification of uncertainty). We sampled directly from the six observed residual aperture values, thereby preserving the empirical variability without imposing distributional assumptions.

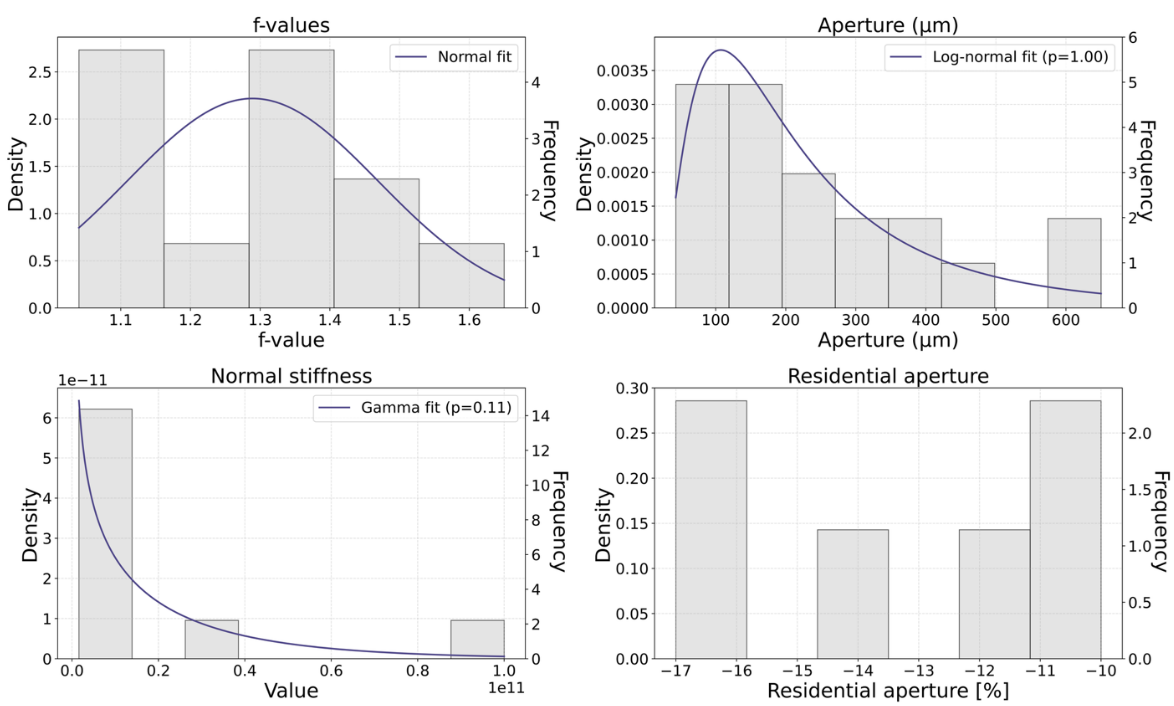

Figure S2. Values and corresponding distributions for roughness factor, aperture, normal stiffness, and residual aperture.

S1.5 Quantification of uncertainty

Each Monte Carlo run used randomly selected values for the parameters initial aperture, effective normal stress (fracture angle), initial normal stiffness, and residual aperture. As described in section 1.3 and 1.4, we applied a normal distribution for the roughness factor, log-normal distribution for the initial aperture, a gamma distribution for the initial normal stiffness and a non-parametric approach for the residual aperture. The effective normal stress on fractures has a high uncertainty because of the unknown angle of the fractures. We randomly assign an angle between 0 and 90, representing the full possible range of fracture inclinations. Finally, permeability samples are generated using an uncertainty range from 0.55 to 3.3. The uncertainty range is based on slug test analysis, where inclusion of non-linear sections in the head–time relation could lead to errors of 80–230%, corresponding to a factor of 0.55–3.3 in permeability estimates (Bouwer & Rice, 1976). We apply this range in log space to generate a log-uniform distribution of possible values.

S1.6 Geological factors influencing porosity

Apart from depth, porosity can be influenced by a number of factors. We test whether fracture porosity is correlated with the following geological variables: surface tectonic setting (Hasterok et al., 2022), type of plate boundary (Hasterok et al., 2022) and rock type. These variables are available for 98% of the dataset, allowing for a robust analysis of their potential influence on porosity. Each variable is categorized. Variable categories with fewer than 150 observations were merged into the ‘other’ category to ensure that each group has enough ranked data to provide meaningful statistical comparisons and stable effect-size estimates.

Each variable will be examined using three analyses and a model: the Kruskal-Wallis test, twice the Mann-Whitney U test (once on raw porosity, once on depth-corrected residuals) and log-log ordinary least squares model. The Kruskal-Wallis test is used to test if the variable contributes to porosity, with the null hypothesis that all groups share the same porosity distribution. The Kruskal-Wallis test was preferred over other tests like ANOVA, because the Kruskal-Wallis test does not assume normality, does not require equal variance and is more robust under skewed distributions (Kruskal & Wallis, 1952). If the Kruskal-Wallis test was significant, meaning at least one of the groups had a different distribution, we applied the Mann-Whitney U test. We tested each variable group versus the other variables combined, which helps us indicate which groups contribute significantly to porosity and differ from the rest. The Mann-Whitney U test, like the Kruskal-Wallis test, is rank-based, making it perfect for skewed data and is not easily influenced by outliers (Mann & Whitney, 1947). We used Holm-Bonferroni correction on the p-values to adjust for multiple comparisons, controlling the family-wise error rate (Holm, 1979).

Furthermore, to estimate if the tested group has often larger or smaller porosity, we used Cliff's delta (δ). It measures how often values in one group are larger than values in another (Cliff, 1993). These effect sizes were interpreted using the thresholds proposed by Romano et al. (2006): $|\delta| < 0.147$ negligible, $0.147 \leq |\delta| < 0.33$ small, $0.33 \leq |\delta| < 0.474$ medium, and $|\delta| \geq 0.474$ large

This Mann-Whitney U test, with Holm-Bonferroni correction and Cliff's delta, determines if the porosity is significantly lower or higher for each group, compared to the other groups. However, it is possible that a difference is found that can be attributed to a different depth range between groups. Therefore, we applied a log-log ordinary least squares model to all the data and found a general depth trend.

$$log_{10}(\mathrm{q}) = \mathrm{b}_0 + \mathrm{b}_1 log_{10}(z) \tag{S15}$$

Next, for each datapoint, we calculated the residual. A positive residual indicates a higher porosity than expected for that depth.

$$residual = log_{10}(q) - (b_0 + b_1 log_{10}(z)) \tag{S16}$$

We rerun the Mann-Whitney U test on these residuals, so we compensate for depth. Comparing the first Mann-Whitney U test and the second one tells us if the difference in porosity distribution can be attributed to depth.

The final tests we applied were a log-log ordinary least squares model, and we calculated the Spearman rank correlation coefficient. The log-log-ordinary least scares model, applied to each variable group, to find individual porosity-depth trends and see how they differ. Some groups may exhibit a faster reduction in porosity with depth than other groups.

$$log_{10}(q) = a_g + b_g log_{10}(z) \tag{S17}$$

To determine if there is a statistically significant relationship between porosity and depth, we calculated the Spearman rank correlation coefficient (ρ) and its associated p-value (Spearman, 1904).

Text S2. Additional results and discussion

S2.1 Geological factors influencing porosity

In addition to depth, several external geological factors can influence porosity in crystalline rock formations. For the geological factors rock type, tectonic setting and plate boundary, we tested if that geological factor has an influence on porosity and if so, how each group contributes to porosity compared to the other groups, after controlling for depth. Finally, we tested how the porosity-depth relationship differs across the geological factors, using log-log regression models with group-specific slopes and intercepts.

Rock type influences porosity, with pegmatite showing the most meaningful deviation from the overall porosity–depth trend. A Kruskal-Wallis test indicates that rock type influences porosity distributions overall ($H(5) = 1777$, $p < 0.001$). After controlling for depth, pegmatite showed the largest positive deviation from expected porosity ($\delta = 0.403$, medium effect), followed by schist and 'other' ($\delta = 0.303$ & $\delta = 0.317$, small effects). Granite, gneiss, and diorite were statistically significant ($p < 0.001$) but had a negligible negative effect ($\delta < 0$), suggesting limited geological importance. Figure S3 shows median of the data points of the first 100 meters of all the data and the median of the specific rock type. This shows that granite, pegmatite, gneiss and diorite have median values very close to the overall median, while schist and 'other' are further apart from the median. To assess how strongly porosity varies with depth within each rock type, we calculated Spearman rank correlations. Schist shows a strong monotonic porosity–depth relationship ($\rho = -0.699$), while granite and the 'other' category show moderate correlations ($\rho = -0.520$ and -0.494, respectively). Gneiss and diorite exhibit only weak correlations ($\rho = -0.268$ and -0.170), indicating that depth plays a comparatively minor role in these lithologies. Pegmatite shows no significant monotonic trend with depth ($\rho = -0.047$, $p = 0.088$), consistent with its positive deviation from expected porosity after depth correction. In addition, Figure S3 shows the log-log regression model with group-specific slopes and intercepts. The model explains approximately 21% of the data variability in log-transformed porosity. Granite and schist show a steeper decline in porosity with depth compared to the overall trend, while the other rock types have a more gradual decline with depth. Although the overall trend shows decreasing porosity with depth for rock types, some sequences display the opposite behavior. This is also observed in Figure S4 and Figure S5. These increases occur where the depth-dependent aperture decreases steeply relative to permeability.

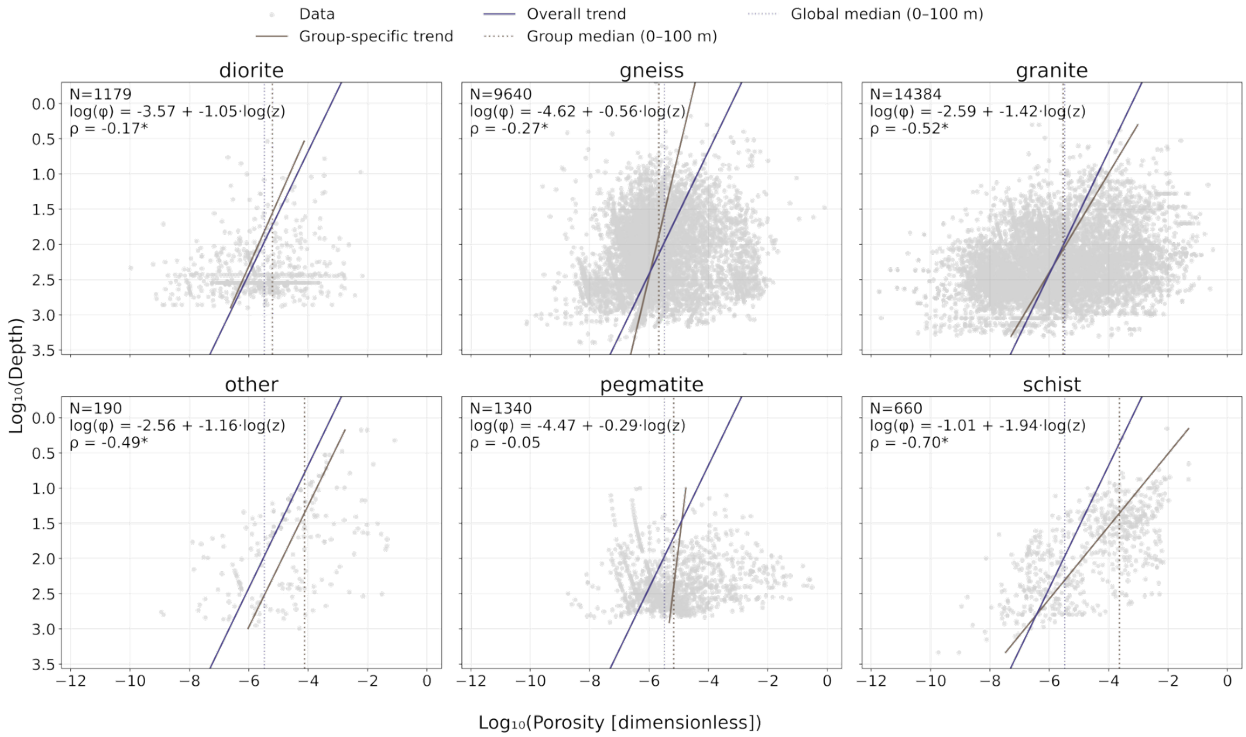

Figure S3. Porosity as a function of depth for each rock type. The solid red line shows the group–specific log–log regression trend, while the solid grey line shows the overall trend. The dotted red line marks the group median porosity within the 0–100 m depth interval, and the dotted grey line marks the global median within the same interval.

Furthermore, geological setting affects porosity, with shields, accretionary complexes, and cratons showing the strongest positive deviations. Geological setting influences the porosity distribution ($H(7)$ =3852, $p < 0.001$). Shield, accretionary complex, and craton show noticeably higher porosity values than the expected porosity (δ = 0.267, 0.202 & 0.257, respectively, small effects). Furthermore, ‘other’ shows a statistically significant ($p <$ 0.001) positive effect on porosity but had a negligible effect size ($\delta < 0.08$). Orogenic belt, magmatic province, volcanic arc, and wide rift all showed the negative deviation ($\delta < 0$) from expected porosity, from which orogenic belt had a small effect and the rest a negligible effect size (δ = -0.173, δ = -0.121, δ =-0.076 & δ =-0.099, respectively). Figure S4 shows a similar pattern looking at just the first 100 meters depth interval medians. Accretionary complex, craton, orogenic belt and shield have a median above overall median, while the other rock types have a median below the overall median. In terms of porosity-depth relationship, we observe steeper strong relationship for orogenic belt (ρ=-0.788), compared to the overall relationship and a very gradual relationship and non-existent monotonic trends for magmatic province and wide rift . The model explains approximately 26% of the data variability in log-transformed porosity.

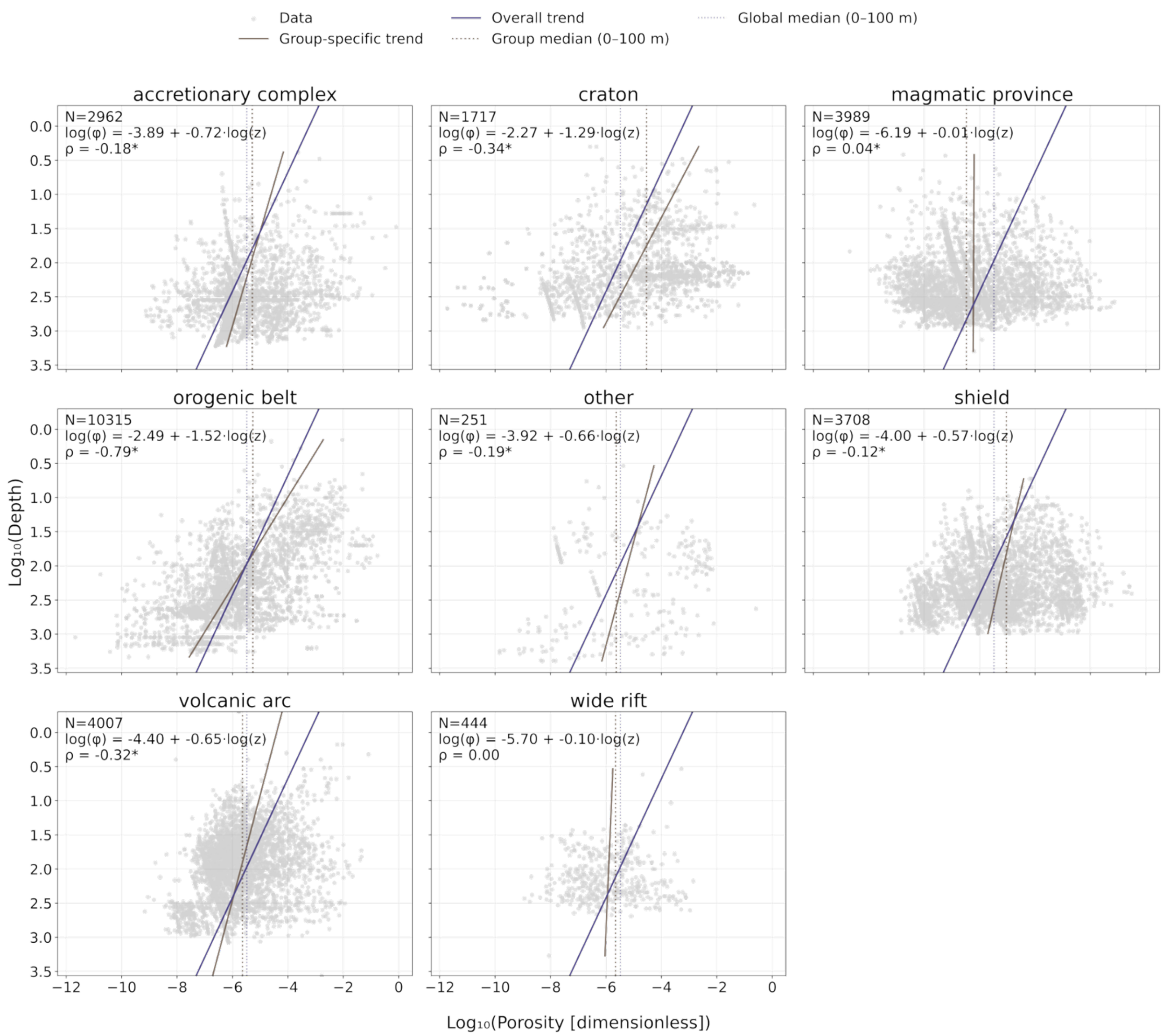

Figure S4. Porosity as a function of depth for each geological setting. The solid red line shows the group–specific log–log regression trend, while the solid grey line shows the overall trend. The dotted red line marks the group median porosity within the 0–100 m depth interval, and the dotted grey line marks the global median within the same interval.

Although plate boundary type appears to affect porosity, depth differences between boundary categories largely determine which effects remain significant. For plate boundary, we have used the plate boundary closest in distance to the permeability measurement point, however it is possible that a measurement point is influenced by another plate boundary type close by. The Kruskal-Wallis test indicates that plate boundary has an influence on porosity and a one versus all analyses shows that all plate boundaries are significant contributors without a depth correction. With a depth correction, only the dextral transform (positive, δ = 286, small effect) and the subduction zone (negative, δ = -0.219, small effect) contribute significantly. The importance of applying a depth correction is evident in Figure S5. The plate boundary types differ substantially in both sample size and depth distribution, with the collision zone containing the largest number of data points. This is also visible when examining the log-log regression model with group-specific slopes and intercepts, which explains 18% of the variability. The collision zone trend is almost identical to the overall trend.

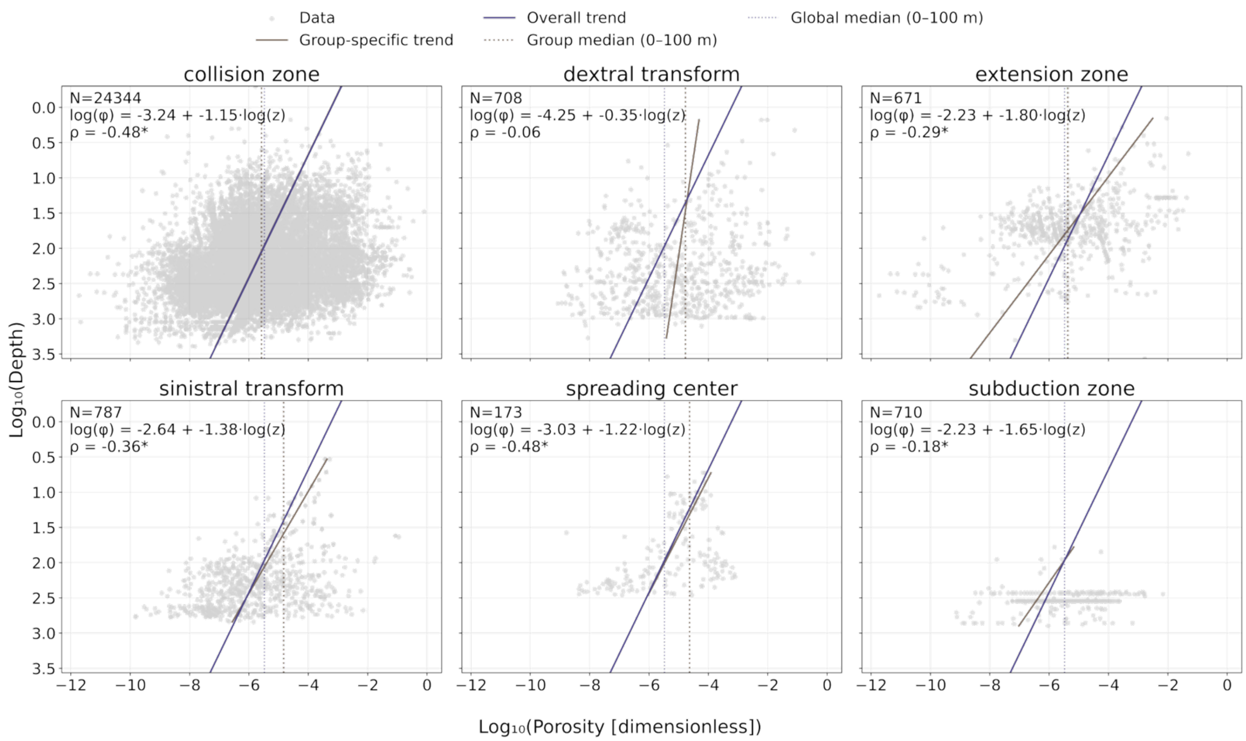

Figure S5. Porosity as a function of depth for plate boundary type. The solid red line shows the group–specific log–log regression trend, while the solid grey line shows the overall trend. The dotted red line marks the group median porosity within the 0–100 m depth interval, and the dotted grey line marks the global median within the same interval.

Some porosity sequences show an apparent increase with depth, a pattern likely driven by model behavior rather than by real geological processes. Figure S3, 4 and 5 show sequences of increasing porosity with depth. This behavior is not expected, as porosity in crystalline rocks generally decreases with depth due to increasing effective stress, which is also reflected in our overall dataset. This is due to a decline in aperture which exceeds the decline in permeability with depth. Because aperture decreases more rapidly with depth than permeability does, the ratio k/b^2 Equation S13 can increase even when permeability itself declines. This is likely a model-driven artifact and not a physical increase. Figure S6shows our aperture decline with depth versus the estimated decline in aperture with effective normal stress from Baghbanan & Jing (2008). Our decline in porosity is much faster for the first kilometer, compared to Baghbanan & Jing (2008), almost 1.74 times.

Beyond that, the rate of decline slows substantially, dropping to only 19% of the Baghbanan & Jing (2008) rate. We adopted the aperture–depth equation from Jiang et al. (2010) based on the availability of the parameters needed (see Text S1.2). The calculation of aperture as a function of depth carries substantial uncertainty. A higher initial normal stiffness or a larger initial aperture would produce a more gradual reduction in aperture with depth, which in turn would yield lower porosity values than those presented here. However, our uncertainty analysis indicates that variations in these parameters have only a modest effect on the median porosity. Although parameter uncertainty influences the absolute magnitude of porosity, the overall depth trend remains stable across all parameter combinations tested. We therefore consider the main patterns reported here to be robust.

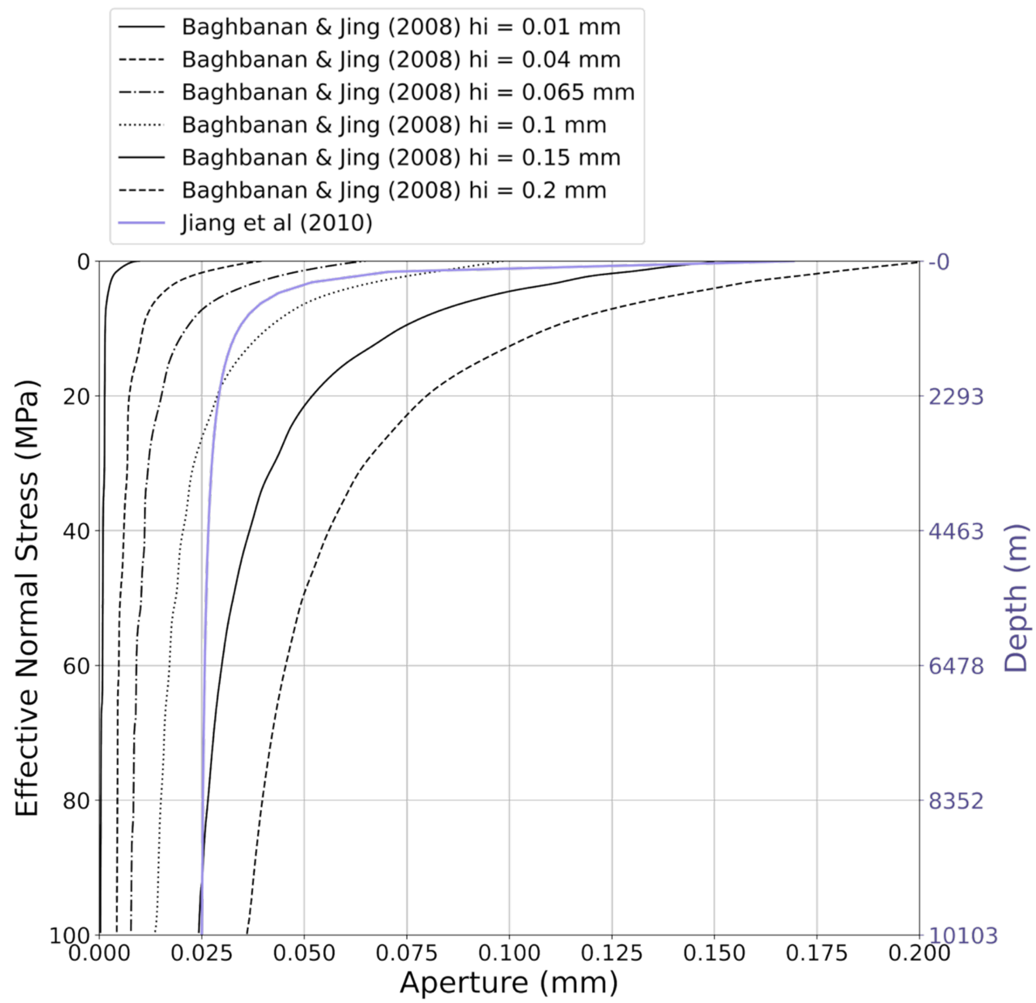

Figure S6. Digitalized variation of aperture with normal stress for assumed initial apertures from Baghbanan & Jing (2008), in black and our aperture with effective normal stress and depth in red.

Although depth remains the dominant control, geological factors are important as well. Our research showed that in particular, rock type and geological setting explain part of the variability in the data. It shows that not all crystalline rocks behave alike. This is also observed by Achtziger-Zupančič et al. (2017) and Ranjram et al. (2015). Both studies conclude that depth is the primary control, but that several geological factors still exert influence. Achtziger-Zupančič et al. (2017) found that lithology has only a small effect on permeability and reported a stronger influence of geological setting than we observe. In doing so, it also removes the connectivity-driven variability in the permeability data and standardizes depth effects, thereby reducing tectonic signals while making small lithology differences more visible. This also removes the much larger connectivity-controlled permeability variations that dominate the geological trends in the Achtziger-Zupančič et al. (2017) study. This filtering effect is why our geological patterns appear weaker overall. Ranjram et al. (2015) also found only a weak effect of lithology, mainly near the surface, and they similarly conclude that tectonic setting is more influential than lithology in the shallow crust.

It is important to note that in our study, each geological factor was tested independently, although their categories may overlap. For example, orogenic belts show a negative deviation from expected porosity, as do gneiss and granite. However, the orogenic-belt group is composed predominantly of granite (73%) and gneiss (22%). Thus, the observed effect for the orogenic belt primarily reflects the lithological composition of that group rather than an interaction between rock type and tectonic setting. Each variable, therefore, represents an isolated comparison, and differences should not be interpreted as additive or combinable across variables.

S2.2 Fracture density

The fracture density distributions are, as are the porosity distributions, highly right-skewed across all depth intervals. Their distribution becomes more compact with increasing depth and do not match common parametric forms. Figure S7 presents fracture density distributions across different depth intervals. Consistent with our porosity analyses, the skewness is evident when comparing mean and median values. In the 0–100 m interval, the median fracture density is $3.50 \text{ x } 10^{-2}$ m^{-1}, while the mean is 244 times higher at 8.54, suggesting the presence of extreme outliers. However, both the absolute IQR and the ratio between median and mean decrease with depth, indicating that the distributions become less variable and slightly less skewed. Suggestion that the distributions become more compact and less influenced by extreme values in deeper intervals.

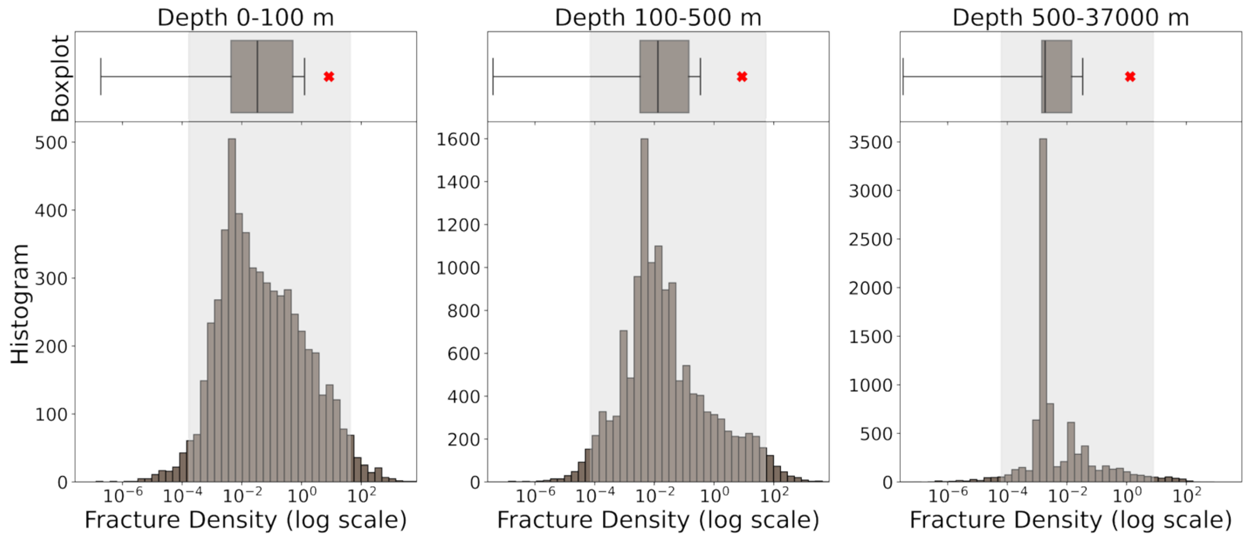

Figure S7. Fracture density distributions across three depth intervals: 0–100 m, 100–500 m, and 500–36,000 m.

References

Achtziger-Zupančič, P., Loew, S., & Mariéthoz, G. (2017). A new global database to improve predictions of permeability distribution in crystalline rocks at site scale. *Journal of Geophysical Research: Solid Earth*, *122*(5), 3513–3539. https://doi.org/10.1002/2017JB014106

Baghbanan, A., & Jing, L. (2008). Stress effects on permeability in a fractured rock mass with correlated fracture length and aperture. *International Journal of Rock Mechanics and Mining Sciences*, *45*(8), 1320–1334. https://doi.org/10.1016/j.ijrmms.2008.01.015

Bouwer, H., & Rice, R. C. (1976). A slug test for determining hydraulic conductivity of unconfined aquifers with completely or partially penetrating wells. *Water Resources Research*, *12*(3), 423–428. https://doi.org/10.1029/WR012I003P00423

Brabazon, J. W., Perfect, E., Gates, C. H., Bilheux, H. Z., Tyner, J. S., McKay, L. D., & Horodecky, B. B. (2019). Rock Fracture Sorptivity as Related to Aperture Width and Surface Roughness. *Vadose Zone Journal*, *18*(1), 1–10. https://doi.org/10.2136/VZJ2018.08.0156

Cheng, Y., & Renner, J. (2022). Estimation of fracture normal stiffness using wellbore pressure recovery. *Geophysical Journal International*, *232*(1), 223–246. https://doi.org/10.1093/GJI/GGAC295

Christensen, N. I., & Mooney, W. D. (1995). Seismic velocity structure and composition of the continental crust: a global view. *Journal of Geophysical Research*, *100*(B6), 9761–9788. https://doi.org/10.1029/95JB00259

Cliff, N. (1993). Dominance statistics: Ordinal analyses to answer ordinal questions. *Psychological Bulletin*, *114*(3), 494–509. https://doi.org/10.1037/0033-2909.114.3.494

Hakami, E. (1989). *RUCI Water Flow in Single Rock Joints SWEDISH NUCLEAR FUEL AND WASTE MANAGEMENT CO Division of Research and Development*.

Hakami, Eva. (1995). *Aperture distribution of rock fractures*. Kungl. Tekniska högskolan.

Hasterok, D., Halpin, J. A., Collins, A. S., Hand, M., Kreemer, C., Gard, M. G., & Glorie, S. (2022). New Maps of Global Geological Provinces and Tectonic Plates. *Earth-Science Reviews*, *231*, 104069. https://doi.org/10.1016/J.EARSCIREV.2022.104069

Holm, S. (1979). A Simple Sequentially Rejective Multiple Test Procedure. *Scandinavian Journal of Statistics*, *6*(2), 65–70.

Ingebritsen, S. E., Sanford, W. E., & Neuzil, C. E. (2006). *Groundwater in Geologic Processes* (2nd ed.). Cambridge University Press. www.cambridge.org

Iwano, M., & Einstein, H. H. (1993). *Stochastic analysis of surface roughness, aperture and flow in a single fracture*. *90*, 54103396. http://onepetro.org/ISRMEUROCK/proceedings-pdf/EUROCK93/All-EUROCK93/ISRM-EUROCK-1993-018/1978203/isrm-eurock-1993-018.pdf

Iwano, M., & Einstein, H. H. (1995). *Hydromechanical Characteristics of a Single Rock Joint*.

Jiang, X.-W., Wang, X.-S., & Wan, L. (2010). Semi-empirical equations for the systematic decrease in permeability with depth in porous and fractured media. *Hydrogeology Journal*, *18*(4), 839–850. https://doi.org/10.1007/S10040-010-0575-3/FIGURES/5

Kolawole, F., & Evenick, J. C. (2023). Global distribution of geothermal gradients in sedimentary basins. *Geoscience Frontiers*, *14*(6), 101685. https://doi.org/10.1016/J.GSF.2023.101685

Kruskal, W. H., & Wallis, W. A. (1952). Use of Ranks in One-Criterion Variance Analysis. *Journal of the American Statistical Association*, *47*(260), 583. https://doi.org/10.2307/2280779

Mann, H. B., & Whitney, D. R. (1947). On a Test of Whether one of Two Random Variables is Stochastically Larger than the Other. *Source: The Annals of Mathematical Statistics*, *18*(1), 50–60.

Ranjram, M., Gleeson, T., & Luijendijk, E. (2015). Is the permeability of crystalline rock in the shallow crust related to depth, lithology or tectonic setting? *Geofluids*, *15*(1–2), 106–119. https://doi.org/10.1111/GFL.12098

Romano, J., Kromrey, J. D., Coraggio, J., & Skowronek, J. (2006). Appropriate statistics for ordinal level data: Should we really be using t-test and Cohen'sd for evaluating group differences on the NSSE and other surveys. *Annual Meeting of the Florida Association of Institutional Research.*, *177*(34).

Singhal, B. B. S., & Gupta, R. P. (2010). Applied hydrogeology of fractured rocks: Second edition. In *Applied Hydrogeology of Fractured Rocks: Second Edition*. Springer Netherlands. https://doi.org/10.1007/978-90-481-8799-7

Snow, D. T. (1968). Rock Fracture Spacings, Openings, and Porosities. *Journal of the Soil Mechanics and Foundations Division*, *94*(1), 73–91. https://doi.org/10.1061/JSFEAQ.0001097

Spearman, C. (1904). The Proof and Measurement of Association between Two Things. *The American Journal of Psychology*, *15*(1), 72. https://doi.org/10.2307/1412159

Witherspoon, P. A., Wang, J. S. Y., Iwai, K., & Gale, J. E. (1980). Validity of Cubic Law for fluid flow in a deformable rock fracture. *Water Resources Research*, *16*(6), 1016–1024. https://doi.org/10.1029/WR016I006P01016

Zhang, Z., & Duan, Z. (2005). Prediction of the PVT properties of water over wide range of temperatures and pressures from molecular dynamics simulation. *Physics of the Earth and Planetary Interiors*, *149*(3–4), 335–354. https://doi.org/10.1016/J.PEPI.2004.11.003